The nonlinear impact of surface forcing changes on bottom water formation and overturning in the Southern Ocean

Jan-Erik Tesdal[1,2], Graeme A. MacGilchrist[1,2], Rebecca L. Beadling[1,2], Stephen M. Griffies[1,2], John P. Krasting[2], Paul J. Durack[3]

[1]Princeton University, Atmospheric and Oceanic Sciences Program, Princeton, NJ, USA
[2]NOAA, Geophysical Fluid Dynamics Laboratory, Princeton, NJ, USA
[3]Program for Climate Model Diagnosis and Intercomparison, Lawrence Livermore National Laboratory, Livermore, California, USA

Key Points:

- Lower limb overturning in two climate models increases with projected changes in winds, weakens with increased Antarctic ice sheet melting.
- The two models disagree on the impact of Antarctic Bottom Water in response to meltwater forcing.
- Accurate representation of Antarctic shelf processes are necessary for robust projection of circulation changes in the deep Southern Ocean.

Corresponding author: Jan-Erik Tesdal, jt7058@princeton.edu

Abstract

Two coupled climate models, differing primarily in horizontal resolution and treatment of mesoscale eddies, were used to assess the impact of perturbations in wind stress and Antarctic ice sheet (AIS) melting on the Southern Ocean meridional overturning circulation (SO MOC), which plays an important role in global climate regulation. The largest impact is found in the SO MOC lower limb, associated with the formation of Antarctic Bottom Water (AABW), which in both models is enhanced by wind and weakened by AIS meltwater perturbations. Even though both models under the AIS melting perturbation show similar AABW transport reductions of 4-5 Sv (50-60%), the volume deflation of AABW south of 30°S is four times greater in the higher resolution simulation (-20 vs -5 Sv). Water mass transformation (WMT) analysis reveals that surface-forced dense water formation on the Antarctic shelf is absent in the higher resolution and reduced by half in the lower resolution model in response to the increased AIS melting. However, the decline of the AABW volume (and its inter-model difference) far exceeds the surface-forced WMT changes alone, which indicates that the divergent model responses arise from interactions between changes in surface forcing and interior mixing processes. This model divergence demonstrates an important source of uncertainty in climate modeling, and indicates that accurate shelf processes together with scenarios accounting for AIS melting are necessary for robust projections of the deep ocean's response to anthropogenic forcing and role as the largest sink in Earth's energy budget.

Plain Language Summary

Recent observations and future projections of shifting wind patterns and increased meltwater from Antarctica suggest multifaceted impacts on the Southern Ocean, which is a primary entry point for excess heat and carbon absorbed by the ocean and thus very relevant to global climate regulation. In this study, two different climate models were used to assess how expected changes in wind and meltwater impacts the production and movement of water masses within the Southern Ocean. Both models respond similarly in terms of the south-to-north movement of abyssal waters, which are the densest waters in the deep ocean. However, the increased meltwater from Antarctica has a much greater impact in one model, such that there is no new formation of abyssal waters, leading to a strong reduction in their volume. Abyssal waters are still formed in the other model, with less volume reduction compared to the former. One major reason for the difference between models is how the system of currents around Antarctica is represented, with more refined currents in the higher resolution model leading to more meltwater and stratification at sites where dense waters are formed. This has major implications for how models project the deep ocean's response to climate change.

1 Introduction

The Southern Ocean (SO) is a key region for the formation and transformation of water masses that are critical to the global meridional overturning circulation (MOC) (Speer et al., 2000; J. Marshall & Speer, 2012). Many advances in our understanding of the global MOC have emphasized the crucial role of SO dynamics (Gnanadesikan, 1999; Lumpkin & Speer, 2007; J. Marshall & Speer, 2012; Talley, 2013). Furthermore, ventilation and circulation in the SO serve as major gateways for heat (Chen & Tung, 2014; Roemmich et al., 2015; Sallée, 2018; Lin et al., 2021), carbon (Caldeira & Duffy, 2000; Sigman et al., 2010; Bernardello et al., 2014; Frölicher et al., 2015) and nutrient (Sarmiento et al., 2004) exchanges between the surface and interior ocean. Given the disproportionately large role the SO plays in modulating the uptake, redistribution, and subsequent storage of oceanic heat and carbon, it is crucial that the SO MOC and the associated water mass transformation (WMT) are accurately represented in climate models. Improved understanding of the SO MOC and WMT and their accurate representation in

ocean models is especially important for transient climate responses on decadal and longer time scales given that changes in the SO MOC and associated water masses due to anthropogenic forcing have major implications for global and regional climate (Sarmiento et al., 1998; Rintoul, 2018).

In a zonally integrated sense, the SO MOC consists of two circulation cells which characterize the major meridional transport pathways connecting the upper and lower limbs of the global MOC (Speer et al., 2000; Sloyan & Rintoul, 2001; Olbers & Visbeck, 2005; Lumpkin & Speer, 2007; Talley et al., 2003; Talley, 2013; Cessi, 2019). The upper limb of the SO MOC consists of southward flowing waters in the deep ocean ($\sim 1000-2000$ m) which enter from the subtropics and are subsequently upwelled in the subpolar SO before being transformed into lighter intermediate waters and exported northward. This cell is driven by strong surface divergence in the presence of persistent westerly winds which push water northward in the surface Ekman layer and pulls dense mid-depth water toward the surface (J. Marshall & Speer, 2012; Speer et al., 2000; Döös & Webb, 1994). A portion of this upwelled water, identified as upper Circumpolar Deep Water (CDW), gains buoyancy through surface heating and freshening and is ultimately subducted northward as Antarctic Intermediate Water (AAIW) or Subantarctic Mode Water (SAMW).

Another branch of southward flowing CDW, the so-called lower CDW, is upwelled to the surface near the Antarctic margins and densified by surface cooling and salinification through brine rejection. A process that is central to the SO MOC's lower limb is the formation of Dense Shelf Water (DSW) in localized regions along the Antarctic shelf. This DSW entrains lower CDW as it cascades down the continental slope, ultimately forming Antarctic Bottom Water (AABW) (A. Orsi et al., 1999; A. H. Orsi et al., 2002). As AABW spreads laterally into the deepest parts of the ocean, slow diapycnal mixing processes reduce its density (C. de Lavergne et al., 2016), transforming a portion of AABW into CDW (Talley, 2013), connecting the lower with the upper limb of the SO MOC. The reader might find it useful to refer to a comprehensive schematic of the relevant overturning cells and transports, for example in Figure 5 of Talley (2013) or Figure 1 in Pellichero et al. (2018).

The dynamical mechanisms described above, which govern the SO MOC, involve wind and buoyancy forcing, both of which are subject to change under anthropogenic climate forcing. In particular, Southern Hemisphere westerlies have intensified and shifted poleward over the past several decades associated with an increasingly positive trend in the Southern Annular Mode (G. J. Marshall, 2003; Fogt & Marshall, 2020), and these trends are projected to continue as the climate warms (Swart & Fyfe, 2012; Goyal et al., 2021). Stronger and poleward-shifted winds have been linked to an invigoration of the upper limb overturning (Hogg et al., 2017) associated with increased ventilation (Russell et al., 2006; Bronselaer et al., 2020) and formation of AAIW and SAMW (Waugh et al., 2013; Downes et al., 2017; Gao et al., 2018; Waugh et al., 2019) as well as enhanced upwelling of CDW (Spence, Griffies, et al., 2014; Hogg et al., 2017). The impacts of projected changes in wind stress on the SO MOC's lower limb remain less explored. However, previous modeling studies suggest a strengthening of the lower limb due to greater AABW formation, mostly in connection with enhanced open-ocean polynya activity near the Antarctica margin relative to baseline simulations (Spence, Sebille, et al., 2014; Hogg et al., 2017; Dias et al., 2021). However, numerical models are often limited in their ability to accurately represent AABW formation, due to insufficient horizontal resolution and a lack of representation of critical overflow processes, leading to an underrepresentation of DSW and a bias towards forming AABW via open ocean deep convection (Heuzé et al., 2015; Dufour et al., 2017; Aguiar et al., 2017; Heuzé, 2021; Mohrmann et al., 2021).

The response of the upper cell to intensified and poleward-shifted winds in model simulations (e.g., Hogg et al., 2017; Downes et al., 2017) is consistent with observational evidence of a strengthening of the upper limb of the SO MOC (Waugh et al., 2013). Such

an agreement suggests that the observed intensification and poleward shift of Southern Hemisphere winds are likely imprinting on the upper limb of the SO MOC, with dynamics consistent with those represented in modeling studies. However, the invigoration of the lower limb of the SO MOC that occurs when observed changes in the surface wind stress field are applied in model simulations (Spence, Sebille, et al., 2014; Hogg et al., 2017; Dias et al., 2021) is inconsistent with the observed weakening of the lower limb of the SO MOC (Rintoul, 2007; Purkey & Johnson, 2010, 2013; Schmidtko et al., 2014; Anilkumar et al., 2015) and contraction of AABW volume (Purkey & Johnson, 2012; Azaneu et al., 2013; van Wijk & Rintoul, 2014; Anilkumar et al., 2021). Such disagreements may suggest that observed trends in the surface wind stress are not presently imprinting on the SO MOC's lower limb, or competing processes may be acting to limit the sensitivity of the lower limb to wind stress changes. Furthermore, Zhang et al. (2019) suggest that the deep SO convection is currently in a weakening phase as part of a multidecadal natural variability in the climate system, which overshadows impacts due to wind changes.

Increased stratification of the upper SO in response to surface warming and freshening (e.g., Haumann et al., 2016) has been linked to reduced AABW production (Sallée et al., 2021; C. d. de Lavergne et al., 2014; Snow et al., 2016; Silvano et al., 2018) and a weakening of the abyssal MOC (Stouffer et al., 2007; Morrison et al., 2015). In particular, substantial Antarctic ice sheet (AIS) mass loss observed in recent decades and associated surface freshening (Rignot et al., 2013; DeConto & Pollard, 2016; Rignot et al., 2019; Smith et al., 2020) is a process that is likely a strong contributor to the increased stratification of the subpolar SO. The potential for AIS meltwater to influence Antarctic sea ice trends (Bintanja et al., 2013; Pauling et al., 2016; Purich et al., 2018), ocean circulation (Moorman et al., 2020), regional and global sea level rise (Menviel et al., 2010; Bronselaer et al., 2018; Golledge et al., 2019; Schloesser et al., 2019) and other climate relevant processes, has motivated an increasing number of studies to constrain the climate impacts of this additional meltwater.

Previous modeling studies investigating the impact of Antarctic meltwater on the SO MOC generally agree on a substantial reduction of AABW formation and a weakening of the lower limb (Fogwill et al., 2015; Lago & England, 2019; Moorman et al., 2020; Mackie et al., 2020), which is consistent with observed changes in the abyssal ocean over recent decades (Lago & England, 2019; Purkey & Johnson, 2013). However, it is unclear how these changes compare to, and are potentially compensated by, perturbations of momentum forcing from enhanced and poleward shifted westerly winds. Modeling studies that used idealized CO_2-only forcing scenarios (Palter et al., 2014; Newsom et al., 2016) or buoyancy perturbation experiments (Stouffer et al., 2007; Morrison et al., 2015) also imply a slowdown in the MOC due to increased stratification. However, these studies have not included additional freshening from AIS meltwater in their forcing protocol, thus the documented MOC response is likely underestimated, particularly the response of the lower limb (Lago & England, 2019).

Studies utilizing idealized perturbation experiments have either focused on the response to wind stress change (Spence, Sebille, et al., 2014; Hogg et al., 2017; Bishop et al., 2016; Downes et al., 2017) or AIS melting individually (Fogwill et al., 2015; Lago & England, 2019; Moorman et al., 2020). However, recent work by Bronselaer et al. (2020) and Beadling et al. (2022), highlight that both the projected wind stress changes and AIS melting are critical to consider together when investigating the transient response of the SO, given their competing effects on SO ventilation and the thermal response on the Antarctic shelf. Previous studies suggest opposing imprints of wind and AIS melt perturbations on SO water masses and circulation, with contributions that are likely not a simple linear combination of separate perturbation responses (Dias et al., 2021; Beadling et al., 2022). This non-linear response precludes the possibility of attributing changes in the SO MOC to individual contributions from AIS melt and wind stress change in previous studies that have not considered both forcings in tandem. Furthermore, the diver-

sity of models and the differing experimental designs of previous perturbation experiments prevents quantifying the uncertainty in changes in the formation and transport of SO water masses in response to wind and meltwater forcings. It is therefore timely to follow up with an idealized perturbation study that focuses on the individual and combined effects of projected wind stress changes and AIS melting, which are highly relevant for future changes of the SO MOC.

The goal of this study is to mechanistically characterize and compare the transient response of the SO MOC to wind stress perturbations and AIS meltwater input expected near the middle of the 21st century in two fully coupled climate models. We provide a description of the two climate models as well as the idealized perturbation experiments and analysis framework in Section 2. Section 3.1 compares the two models based on their mean representation of the SO MOC and its anomalies in the perturbation experiments. Here we show that the change in AIS melting has the dominant impact on the combined response to forcing, where both models exhibit a clear weakening of the lower limb circulation. In Section 3.2 we use a water mass transformation framework to describe how surface buoyancy modification from AIS melting corresponds to changes in the SO interior in the form of both water mass volume change and overturning. The water mass transformation analysis highlights crucial differences between the two models that are not apparent in the MOC response. Furthermore, since the two models have important differences regarding spatial resolution and mesoscale eddies, this comparison helps to mechanistically understand how model uncertainty can imprint on SO MOC changes resulting from changes in buoyancy forcing. We further discuss these results in Section 4 with a summary and conclusion offered in Section 5.

2 Methods

2.1 Models

We use a fully-coupled numerical global climate model (CM4, (Held et al., 2019)) and Earth system model (ESM4, (Dunne et al., 2020)) developed at the Geophysical Fluid Dynamics Laboratory (GFDL) of the National Oceanic and Atmospheric Administration (NOAA) and contributed to the sixth phase of the Coupled Model Intercomparison Project (CMIP6; Eyring et al., 2016). As both models share many characteristics, we review similarities and key differences relevant for the SO. We limit our description here to the ocean and sea ice components in each model as Beadling et al. (2022) and references therein, including Held et al. (2019) and Dunne et al. (2020), provide complete model component descriptions for CM4 and ESM4.

Both CM4 and ESM4 have a fully coupled atmosphere, land, ocean and sea ice components. The ocean and sea ice model (GFDL-OM4.0, (Adcroft et al., 2019)) is based on version 6 of the Modular Ocean Model (MOM6) code. A key change of MOM6 from previous versions is the implementation of the Arbitrary Lagrangian-Eulerian (ALE) algorithm, along with a vertical Lagrangian remapping method, thus enabling a full generalization of the vertical coordinate (S. Griffies et al., 2020). In both models, the vertical coordinate in OM4 is a hybrid between potential density (rho2, referenced to 2000 dbar) at depth and re-scaled geopotential (z^*) in the upper ocean (spacing varying from 2 m near the surface to 20 m before transitioning to isopycnal coordinates at $\sim$200 m). In both models, the vertical coordinate is comprised of 75 hybrid layers spanning the entire water column (0-6500 m). The z^* coordinate in the upper ocean is more appropriate because the resolution in isopycnal space breaks down in the absence of vertical stratification within the mixed layer. In the interior, the preference for isopycnal coordinates is motivated by the preservation of interior water masses and the improved representation of circulation that predominantly occurs along isopycnals. The implementation of the hybrid coordinate reduces the occurrence of spurious diapycnal mixing that has been a common problem in pure vertical z^* grid models (S. M. Griffies et al., 2000; Adcroft

et al., 2019) and improves representation of overflows (Legg et al., 2006) which is relevant for the SO.

The horizontal grid spacing of the ocean/sea ice component differs between the two models, with a nominal horizontal grid spacing at 0.25° and 0.5° in CM4 and ESM4, respectively. Another major difference is that the higher horizontal resolution ocean component in CM4 does not include a mesoscale eddy parameterization, while ESM4 employs the Mesoscale Eddy Kinetic energy parameterization (MEKE) to represent subgridscale eddy processes (Redi, 1982; Gent et al., 1995; D. P. Marshall & Adcroft, 2010). CM4 can be regarded as "eddy permitting", as a horizontal grid spacing of 0.25° resolves eddies in the tropics and subtropics, but incompletely at high latitudes. During the development phase, it was found that the 0.25° version of OM4 offered a better simulation with no mesoscale eddy parameterizations, based on several climate relevant metrics such as sea surface temperature biases (Adcroft et al., 2019; Held et al., 2019). However, that conclusion is the subject of ongoing research to develop suitable scale-aware mesoscale eddy parameterizations (e.g., Jansen & Held, 2014). Both models, however, include a parameterization for the restratification effects of submesoscale eddies. The strength of this parameterization differs slightly between the two models, with ESM4 being tuned to have slightly stronger restratification from submesoscale eddies (Dunne et al., 2020; Adcroft et al., 2019).

While ESM4 retains most of the baseline configuration of CM4, viscosity was enhanced in the SO (up to 2000 $m^2\ s^{-1}$) to maintain the propagation of ventilated waters away from the Antarctic continent (Dunne et al., 2020). This modification suggests that the interior mixing term is crucial in understanding potential differences in ESM4 and CM4 regarding the meridional overturning and ventilation in the SO. Both CM4 and ESM4 employ the SIS2.0 sea ice model with five thickness layers and the same horizontal grid spacing as their MOM6 configuration. As detailed by (Dunne et al., 2020), ESM4 has higher sea ice and snow-on-glacier albedos compared to CM4, which serve to maintain a surface climate in ESM4 more appropriate for the representation of coastal polynyas around Antarctica, and in turn to prevent unrealistic subsurface heat build up ((see also Delworth et al., 2020).

Other important differences between the models relate to the representation of aerosols and atmospheric chemistry, which can influence the simulated ventilation in the SO (Dunne et al., 2020). For example, atmospheric sea salt is approximately five times higher in CM4 than in ESM4, leading to reduced cloud cover in the latter model. Ozone, which determines the strength of the polar vortex, is interactive in ESM4 but prescribed in CM4. The representation of sulfate aerosols, which increase the amount of incident shortwave radiation over the SO, also differs between the models, with ESM4 parameterizing sulfate explicitly while CM4 does so implicitly. The interested reader may refer to Table 1 in (Dunne et al., 2020) for further details on comparing the CM4 and ESM4 models.

2.2 Experimental Design

We investigated the steady-state connections between WMT, MOC, and ocean ventilation in the SO and their transient response to idealized freshwater and wind stress perturbations. The perturbation experiments are designed to represent the increased melting of the Antarctic Ice Sheet (AIS) and an increase and poleward shift of the Southern Hemisphere westerlies projected to occur near the middle of the twenty-first century under a high emissions scenario (Beadling et al., 2022; DeConto & Pollard, 2016; Gregory et al., 2016). The four experiments analyzed in this study include (1) the previously spun-up pre-industrial control (piControl) simulation contributed to CMIP6 (Eyring et al., 2016) (referred to hereafter as Control), (2) an experiment with a 0.1 Sv freshwater perturbation entering at the Antarctic coast (referred to hereafter as Antwater), (3) an experiment imposing zonal and meridional wind stress perturbations (referred to here-

after as Stress), and (4) an experiment that simultaneously imposes the freshwater and momentum perturbations (referred to as AntwaterStress). All perturbation experiments branch from each model's Control integration. The experiments in this study are identical to those described in Beadling et al. (2022) and readers are referred to the experimental design described therein, but we summarize several key points here.

In Antwater, a constant meltwater flux enters the ocean surface at sea surface temperature (SST) within a 1° latitude band extending from the Antarctic coast in regions of observed ice shelf melting (Paolo et al., 2015). Thus, freshwater forcing is not spatially uniform, but applied in regions where ice shelf mass loss is prevalent (i.e, the majority enters along the West Antarctic Peninsula and the West Antarctic continental shelf). The total freshwater transport from ice shelf melt is scaled to 0.1 Sv, which corresponds to the magnitude of the total meltwater flux from the AIS near mid-century (year 2037) as projected from recent dynamic ice-sheet model simulations under the CMIP5 Representative Concentration Pathway 8.5 Scenario (RCP8.5) (DeConto & Pollard, 2016). Under RCP8.5, atmospheric CO_2 concentrations are approximately doubled near the middle of the 21st century relative to preindustrial (Riahi et al., 2011). Thus, the 0.1 Sv magnitude pairs well with the Flux-Anomaly-Forced Model Intercomparison Project (FAFMIP) wind stress perturbations (Gregory et al., 2016) described below which are derived from projected changes at the time of CO_2 doubling.

The Stress experiment imposes global perturbations in the zonal and meridional momentum flux (i.e., wind stress) at the ocean surface, which directly corresponds to the "faf-stress" perturbation described in Gregory et al. (2016). Relative to their Control fields, these perturbations result in an 8-9% increase in the strength of the maximum zonal-mean wind stress over the SO and a ∼1° poleward shift in CM4 and ESM4. In FAFMIP, these perturbations are derived from the projected changes that occur at the time of CO_2 doubling (response centered on years 51-70) in 1pctCO2 simulations from an ensemble mean of 13 CMIP5 models (Gregory et al., 2016).

The AntwaterStress experiment imposes the Antwater and Stress perturbations simultaneously. Both the Stress and AntwaterStress experiments follow the CMIP6 FAFMIP protocol, which prescribes isolated surface flux perturbations to characterize a model's response to surface forcings projected under a doubling of atmospheric CO_2 relative to pre-industrial conditions (Gregory et al., 2016). Following Beadling et al. (2022), our AntwaterStress experiment uses the same protocol as "Antwater-Stress" described in FAFMIP. However, we omit the dash, "-", to avoid misinterpretation as "Antwater minus Stress". The Antwater experiment applies the same freshwater forcing as AntwaterStress, but does not include the wind stress perturbation.

Three ensemble members branching from the corresponding Control integration were performed for each perturbation experiment, each with a simulation length of 70 model years. Given the documented multidecadal to centennial scale variability that characterizes the SO piControl state in both models (Held et al., 2019; Dunne et al., 2020), the response to each perturbation can be dependent on the underlying ocean state at the time of experiment initialization (i.e., piControl branch point). The internal variability is largely derived from deep convective events associated with open ocean polynyas in the Ross and Weddell Seas and has been documented in other versions of GFDL models (e.g., Zhang et al., 2017, 2019, 2021, 2022). Thus, the branch points for each ensemble member were strategically selected in relation to the life cycle of the polynya events – i.e. the oceanic heat build-up, release, and recovery phases – in order to capture different aspects of SO variability internal to the control runs.

To ensure a robust signal with minimal influence from internal variability, when assessing the response, we compute differences relative to a 100-year period in the Control integration that overlaps with the time period of each model's ensemble members. Unless otherwise noted, analysis is done on the ensemble mean, with which the response

to the perturbation is evaluated by subtracting the 100-year Control mean from the last 20 years of each perturbation experiment (average of years 51 to 70).

In CM4, we selected a time period spanning simulation years 251 to 400, with a polynya event occurring near year 330 in the Ross Sea. The three ensemble members branch from years 251 (∼70 years before the polynya), 290 (∼40 years before the polynya), and 332 (during the polynya). The 100-year time period of the Control run to compare to the perturbation runs is from simulation years 281 to 380. In ESM4, polynyas are more frequent compared to CM4 (occurring at years 110 and 215 in the Ross Sea and year 240 in the Weddell Sea). The three ensemble members branch from years 101 (10 years before a polynya), 151 (50 years after and 65 years before a polynya), and year 201 (10 years before a polynya). These branch points correspond to the same branch points used for the CMIP6 historical simulations for ESM4 (Dunne et al., 2020). The 100-year time period of the Control run to compare to the perturbation runs is from simulation year 121 to 220.

2.3 The WMT framework

This study uses the WMT framework to investigate how the SO deep water masses respond to changes in surface buoyancy fluxes. The WMT framework was initially put forward by Walin (1982) to describe the relationship between surface heat fluxes and interior ocean circulation. A series of studies further refined the framework to include the effect of haline-driven buoyancy forcing (e.g., Tziperman, 1986; Speer & Tziperman, 1992), to apply it to specific regions such as the North Atlantic (e.g., Marsh, 2000; Bryan et al., 2006; Grist et al., 2009, 2012, 2014) or Southern Ocean (e.g., Marsh et al., 2000), as well as account for the role of interior mixing (e.g., Nurser et al., 1999; Iudicone et al., 2008). We refer interested readers to Groeskamp et al. (2019) for a comprehensive overview of past studies in WMT and details of how WMT is derived from diapycnal processes. The methodology is summarized below using the same concepts and notation presented in Groeskamp et al. (2019), but focused on the SO, using potential density referenced at 2000 dbar (σ_2) to classify SO water masses.

A volume budget in isopycnal space can be defined in which the volume (V) below an isopycnal surface (S) for an arbitrary chosen density is controlled by a balance between diapycnal volume transports due to WMT and meridional volume transports due to the SO MOC. This budget is schematically represented in Figure 1 for the zonally-integrated SO. We define the northern boundary of the SO at a given latitude ϕ, in this case ϕ=30°S, in line with the majority of previous water mass analyses in models (e.g., Downes et al., 2011) and observational data (e.g., Talley, 2008, 2013). The rate of change in the volume below the S interface and south of ϕ=30°S, dV/dt, is equal to the total WMT south of ϕ=30°S (G) and the overturning in density space at ϕ=30°S (ψ):

$$\frac{dV}{dt} = G + \psi. \tag{1}$$

The equation above defines a volume balance in the WMT framework, distinguishing overturning at the northern boundary of the Southern Ocean (ψ) from the total transformation (G) and the storage change (dV/dt) within the Southern Ocean. By convention, a positive (negative) dV/dt denotes an inflation (deflation) of the layer volume. If G is positive (negative), seawaters are being densified (lightened), crossing S to denser (lighter) classes and thus adding (removing) volume to the region denser than S. Similarly, positive (negative) ψ denotes integrated volume import (export) across the northern boundary (ϕ=30°S), adding (removing) volume to the region denser than the S interface. At any density, the import (export) and formation (destruction) of a water mass can be calculated as the negative (positive) difference in density space of the three terms in equation (1).

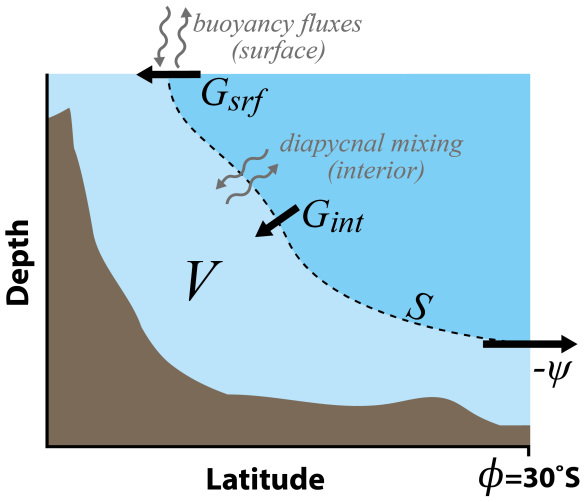

Figure 1. Schematic of the isopycnal volume budget for the zonally-integrated SO. The volume below a given isopycnal surface (S) and poleward of latitude, ϕ, is controlled by three general mechanisms. (1) The surface WMT (G_{srf}) arising from the surface buoyancy fluxes that leads to movement of the isopycnal layer interface, S, thus altering the volume of fluid within the layer. (2) Interior WMT (G_{int}), arising from the volume flux across S by diapycnal mixing. (3) The isopycnal overturning circulation at latitude ϕ (ψ), representing the volume transport across ϕ and below S. Our convention is such that $\psi > 0$ reflects the integrated transport of water away from the region south of ϕ.

Diagnostically, we estimate the volume time tendency, dV/dt, by computing the temporal derivative of ocean model grid-cell volume mapped into isopycnal space. The integrated transport, ψ, is defined as the isopycnal overturning at latitude ϕ and derived from the SO MOC streamfunction, Ψ, which is calculated as

$$\Psi(\phi, \sigma_2) = \int_{\sigma_2^{max}}^{\sigma_2} \int_x v(x, \phi, \sigma_2')\, dx\, d\sigma_2' \tag{2a}$$

$$\psi(\sigma_2) \equiv \Psi(\phi = 30°\mathrm{S}, \sigma_2), \tag{2b}$$

where v is the meridional transport defined at each longitude (x), latitude (ϕ) and density (σ_2), comprising both resolved and eddy-induced components. Ψ is calculated by integrating v from the densest isopycnal (σ_{max}) to the given σ_2, using zero bottom condition at σ_{max} and assuming monotonically increasing σ_2 with depth. Thus, ψ in Figure 1 represents the cumulatively summed volume transport (with units Sv $= 10^6$ m^3 s^{-1}) across ϕ and below S. Note that both the ocean grid-cell volume and the meridional transports need to be defined in isopycnal coordinates (here σ_2) instead of geopotential coordinates to be compatible with the WMT framework, which then has the advantage of directly linking water mass characteristics (i.e., σ_2 range) with processes that lead to the formation or destruction of water masses (e.g., Stewart & Thompson, 2015; Newsom et al., 2016; Groeskamp et al., 2019). Since both CM4 and ESM4 are run with MOM6, we leveraged its online remapping capability to output the grid-cell volume for 35 isopycnal layers in ρ_2 space, spanning 997 to 1039 kg m^3 ($\rho_2 = \sigma_2$+1000 kg m^{-3}, units henceforth dropped). Using the isopycnal volume and transports directly from the model's diagnostic output has the advantage of minimizing any errors associated with time-averaging when binning the grid-cell volume from depth to density space offline (Adcroft et al., 2019). Using online-calculated isopycnal volumes requires evaluation of all terms in Equation (1) in σ_2 space. This approach avoids errors due to time averaging by capturing nonlinear

correlation and allows us to use annually averaged diagnostics of isopycnal transport and grid-cell volume. Furthermore, σ_2 is shown to closely follow neutral density surfaces (Lee & Coward, 2003).

Following (Groeskamp et al., 2019), G is calculated from the integrated material time tendencies of σ_2:

$$G = \frac{\partial}{\partial \sigma_2} \iiint_V \frac{D\sigma_2}{Dt}\, dV. \tag{3}$$

In Figure 1, G is decomposed into WMT due to surface forcing (G_{srf}) and interior diabatic processes (G_{int}). The surface transformation term G_{srf} is evaluated based on knowledge of the surface buoyancy fluxes. In this study, we calculated G_{srf} by integrating the surface density flux (F_{srf}) over the area of the isopycnal outcrop (A):

$$G_{srf} = \frac{\partial}{\partial \sigma_2} \iint_A F_{srf}(x, \phi)\, dA. \tag{4}$$

Using discrete σ_2 classes, based on specific bin widths (here we use a constant bin size of $\Delta\sigma_2 = 0.05$ kg m^{-3}), Equation (4) gives the volume transport across each σ_2 class due to F_{srf}. In turn, F_{srf} is calculated from surface heat (F_Q), salt (F_S) and freshwater (Q_m) fluxes

$$F_{srf} = -\frac{\alpha}{C_p} F_Q + \beta\, [F_S - Q_m\, SSS)], \tag{5}$$

where C_p is the specific heat capacity of seawater, SSS the sea surface salinity; α and β are the thermal expansion and haline contraction coefficients, respectively.

All terms in Equation (5) are common diagnostic model outputs and defined for the top-most model grid layer ($z \approx 2\ m$) as monthly averages. In contrast, the interior transformation term, G_{int}, arises from tendencies associated with interior mixing processes, which are often not available in standard model output. Therefore, as in previous studies (e.g., Downes et al., 2011; Newsom et al., 2016; Cerovečki et al., 2013), we infer G_{int} using the relationship in Equation (1), such that

$$G_{int} = \underbrace{\frac{dV}{dt} - \psi}_{\text{total WMT}} - G_{srf}. \tag{6}$$

That is, we explicitly diagnose the total WMT, $dV/dt - \psi$, as well as the surface transformation, G_{srf}, while G_{int} is inferred. By recognizing that $G = G_{srf} + G_{int}$, any difference between G_{srf} and the total WMT G is ascribed to the WMT due to interior processes, G_{int}, as per equation (6). Although G_{int} mostly represents WMT due to mixing in the interior ocean, we note that WMT due to shortwave penetration (Groeskamp & Iudicone, 2018) and geothermal heat flux (Davies, 2013) are also accounted for in the G_{int} term.

3 Results

3.1 Meridional overturning circulation

3.1.1 Mean-state representation

The SO MOC, as represented by the zonally integrated streamfunction, Ψ from equation (2a), is similar among the CM4 and ESM4 control runs in terms of overall structure and strengths of the different circulation cells (Figure 2). The two models are overall consistent with other studies such as Döös and Webb (1994), Hirst and McDougall (1998), Farneti et al. (2015), Newsom et al. (2016), Cessi (2019), and Urakawa et al. (2020). Notably, we here see a lower cell of counterclockwise circulation (negative Ψ for $\sigma_2 > 36.8$), upper cell of clockwise circulation (positive Ψ between $36.8 > \sigma_2 > 35.5$) and counterclockwise subtropical cell (negative Ψ for $\sigma_2 > 35.5$).

Table 1. Circumpolar mean density ranges in σ_2, volume transports at 30°S, surface and interior formation south of at 30°S for key Southern Ocean water masses in CM4 and ESM4: thermocline water (TW), Subantarctic Mode Water (SAMW), Antarctic Intermediate Water (AAIW), Circumpolar Deep Water (CDW) and Antarctic Bottom Water (AABW). Note that in the circumpolar mean, North Atlantic Deep Water (NADW) is considered part of the CDW. Note that the uncertainties in transports and formation are presented as ± 1 standard deviations derived from the annual means over the given 100-year time periods.

Model	Water mass	σ_2 range (kg m^{-3}-1000)	Vol. transp. (Sv)	Surf. form. (Sv)	Int. form. (Sv)
CM4	TW	$\sigma_2 < 35.60$	0.3 ± 2.0	7.5 ± 3.2	-7.0 ± 4.0
	SAMW	$35.60 \leq \sigma_2 < 36.10$	12.7 ± 1.1	13.7 ± 4.3	-1.3 ± 4.9
	AAIW	$36.10 \leq \sigma_2 < 36.60$	7.0 ± 1.2	-8.7 ± 5.3	13.5 ± 6.2
	CDW	$36.60 \leq \sigma_2 < 37.06$	-24.2 ± 1.9	-23.2 ± 3.7	2.1 ± 5.0
	AABW	$\sigma_2 \geq 37.06$	7.5 ± 1.9	10.7 ± 1.5	-6.4 ± 3.8
ESM4	TW	$\sigma_2 < 35.20$	-6.1 ± 2.5	-8.0 ± 3.7	1.9 ± 4.0
	SAMW	$35.20 \leq \sigma_2 < 35.60$	12.0 ± 2.0	8.9 ± 3.8	4.1 ± 3.8
	AAIW	$35.60 \leq \sigma_2 < 36.50$	5.2 ± 1.5	15.6 ± 5.8	-9.0 ± 5.8
	CDW	$36.50 \leq \sigma_2 < 37.03$	-20.8 ± 2.3	-24.0 ± 3.8	3.3 ± 7.0
	AABW	$\sigma_2 \geq 37.03$	8.0 ± 1.7	7.5 ± 1.2	0.6 ± 6.3

In both models, the lower cell is constrained to a narrow density range at around $\sigma_2 = 37 \pm 0.1$, which resembles the lower limb overturning associated with the formation and transport of AABW. The lower limb circulation strength can be quantified as the minimum of Ψ within the subpolar range of the lower cell south of 55°S (Newsom et al., 2016). In both models, the minimum in Ψ is located at around 65°S with values of -19.3±2.7 Sv and -18.2±3.0 Sv for CM4 and ESM4, respectively. Based on the minimum of the 100-mean Ψ, CM4 has a slightly greater lower cell strength compared to ESM4, but this difference is not significant given that both estimates lie within their year-to-year variability (based on the standard deviation of annual means).

The export of AABW at 30°S is similar between the two models (7.5 ± 1.9 and 8.0 ± 1.7 Sv in CM4 and ESM4, respectively; Table 1). When reprojecting the isopycnal overturning to depth space, we can see that the lower counterclockwise circulation cell occupies most of the subpolar SO with the minimum occurring at around 1000-1500 m depth (Figure 2c,d). Based on the zonal mean density structure (green contours in Figure 2c,d), waters associated with the lower limb overturning are denser in CM4 equatorward of 50°S (based on the height of the 37.0 isopycnal). However, the deep subpolar SO south of 50°S is denser in ESM4 compared to CM4 (based on the height of the 37.1 isopycnal).

The southward flow of the lower cell consists of NADW and lower CDW, which enter the SO and are upwelled in the subpolar latitudes (50-60°S) where they are transformed to either lighter intermediate water masses (AAIW and SAMW) or denser bottom water (AABW). NADW flowing into the SO at 30°S is slightly stronger in CM4 (20.7 ± 0.9 Sv) than in ESM4 (18.8 ± 0.8 Sv). The volume transport of CDW across the Indo-Pacific at 30°S is 3.6 ± 1.6 Sv in CM4 and 1.5 ± 2.1 Sv in ESM4, yielding a total CDW import at 30°S of 24.3 ± 1.9 Sv in CM4 and 20.3 ± 2.3 Sv in ESM4 (Table 1). The transformation of these deep ocean water masses to lighter intermediate water masses comprises the upper overturning cell, which occurs over a much wider density range ($35 < \sigma_2 < 37$) and is situated north of 60°S at 500-2000 m depth. The total export of intermediate waters at 30°S are 19.7 Sv ± 1.6 Sv in CM4 and 17.2 Sv ± 1.7 Sv in ESM4 (Table 1). The smaller transports in ESM4 are consistent with a slightly weaker upper overturning cell in ESM4 compared to CM4 (Figure 2) with the northward transport of intermediate water masses being extended to lighter densities. Possibly related is the anticlockwise cell in the upper SO between 40-60°S which is more pronounced in CM4.

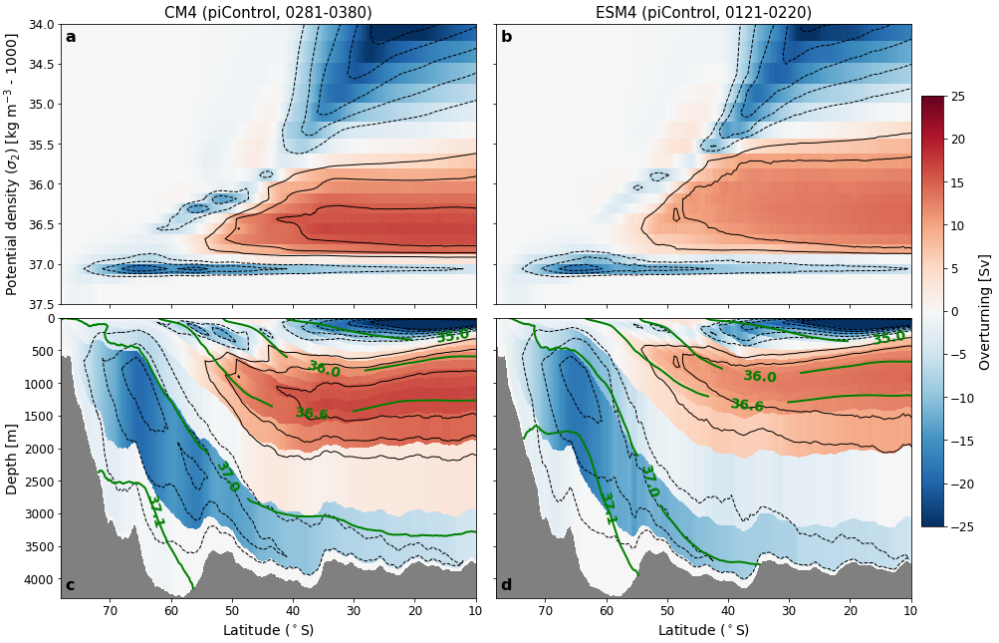

Figure 2. Overturning streamfunction (Ψ) in the Southern Ocean (south of 10°S) in the CM4 (0.25°) and ESM4 (0.5°) Control runs time-averaged over 100-year periods (model years 0281-0380 for CM4 and 0121-0220 for ESM4). Overturning circulation is presented in terms of volume transport (1 Sv = 10^6 m^{3}s^{-1}). Upper panels (a) and (b) show overturning circulation along surfaces of constant density (i.e., isopycnal overturning). Density space is presented in potential density referenced to 2000 dbar (σ_2) and here shown over the range 34 to 37.5 kg m^3, which comprise the density range found in the SO (south of 30°S). Lower panels (c) and (d) show overturning circulation as a function of zonal mean depth of the σ_2 surfaces. We also present some zonal mean potential density contours (green contours) for context. In all panels, positive Ψ (red shading) indicates clockwise circulation and negative Ψ (blue shading) indicates counter-clockwise circulation. Black contours represent the streamfunction in 5 Sv increments and outline the different overturning cells.

Despite these differences, both models agree fairly well with the overall representation of SO overturning. Based on a transport balance across 30°S, in both models the majority of the southward flowing CDW is transformed to intermediate waters with a smaller part transformed to AABW. This transformation matches with estimates by Downes et al. (2011) which evaluated SO water masses in previous generations of GFDL climate models. Although it is not the focus of this study, we note the consistent counterclockwise circulation of the subtropical cell between the two models. This circulation is predominant north of 40°S for the lightest densities ($\sigma_2 < 35$) and is constrained to the upper 500 m.

3.1.2 Changes in response to wind and Antarctic melt perturbations

In Figure 3 we present the response in the SO MOC as anomalies of Ψ based on the final 20 years of the Stress, Antwater, and AntwaterStress experiments. The anomalies are calculated from the average over years 51-70 in the three-member ensemble mean of each perturbation minus the 100-year average of the Control run evaluated in the previous section. Both CM4 and ESM4 show distinct changes in Ψ in response to each perturbation. By far the greatest changes occur in the high density ranges corresponding to the lower cell, with smaller changes seen in the upper cell. As described in Section 2.2, initializations vary between the three ensemble members, such that anomalies due to internal variability are largely averaged out in the ensemble mean so that changes seen in Figure 3 can be considered robust for the given perturbation.

The Stress perturbation leads to a clear strengthening of the lower limb circulation. This strengthening is seen as negative anomalies in Figure 3, which means that the lower cell becomes more negative in the perturbation experiments. In the case of CM4, the minimum in Ψ over the subpolar range is not significantly different from the control run (-20.0±3.8 Sv compared to -19.3 Sv in the Control), but the subpolar cell becomes more negative further equatorward (Figure 3). In the case of ESM4, we see a strengthening of ∼2 Sv (from -18.2 Sv in the Control to -20.4±0.3 Sv) (Note that the ± standard deviation range for the perturbation experiments is based on the variability within the three ensembles, while the ± standard deviation range of the Control is based on the year-to-year variability over the 100-year period). The more striking change in Stress is a shift of the lower cell towards more negative values (by 3 to 6 Sv) north of the minimum (north of 60°S), which indicates that the lower cell becomes more extensive and stronger outside of the subpolar SO. This shift is more pronounced in ESM4 compared to CM4. Compared to this large change in the lower cell, there is a small reduction in the upper cell strength in ESM4 (defined as the maximum in Ψ for $36.7 < \sigma_2 < 35.5$), where the maximum Ψ in ESM4 declines by ∼2 Sv (from 13.0 Sv to 11.2±0.7 Sv). There is no noticeable change in the upper circulation cell in the case of CM4. The relatively small changes in the upper circulation cell suggests compensatory effects mediated by eddy fluxes (Farneti et al., 2010; Farneti & Delworth, 2010; Farneti & Gent, 2011; Gent & Danabasoglu, 2011). Based on analysis focusing on the difference between the ocean components of the two coupled models (Adcroft et al., 2019), it is inferred that CM4 exhibits a more eddy compensated response compared to ESM4.

The Antwater perturbation leads to a weaker lower limb circulation in both models, seen as positive anomalies for σ_2 greater than 36.7. The bottom cell strength in CM4 reduces by 50% (from -19.3 Sv to -9.8±1.4 Sv). In the case of ESM4, the minimum Ψ in the bottom cell reduces by 36% (from -18.2 Sv to -11.7±0.8 Sv). Thus, the impact of Antarctic ice shelf melting on bottom cell strength is greater in CM4 compared to ESM4, reducing by 9.5 Sv in CM4 and only by 6.5 Sv in ESM4. The weakening in the lower limb overturning is strongest in the subpolar region, but the reduction can be seen at all latitudes of the SO (Figure 3). On the other hand, Antwater leads to a slight strengthening of the upper limb overturning. The maximum Ψ in the upper cell increases by 21% (from 16.8 Sv to 20.3±0.3 Sv) in CM4, and by 12% (from 13.0 Sv to 14.6±0.4 Sv) in ESM4.

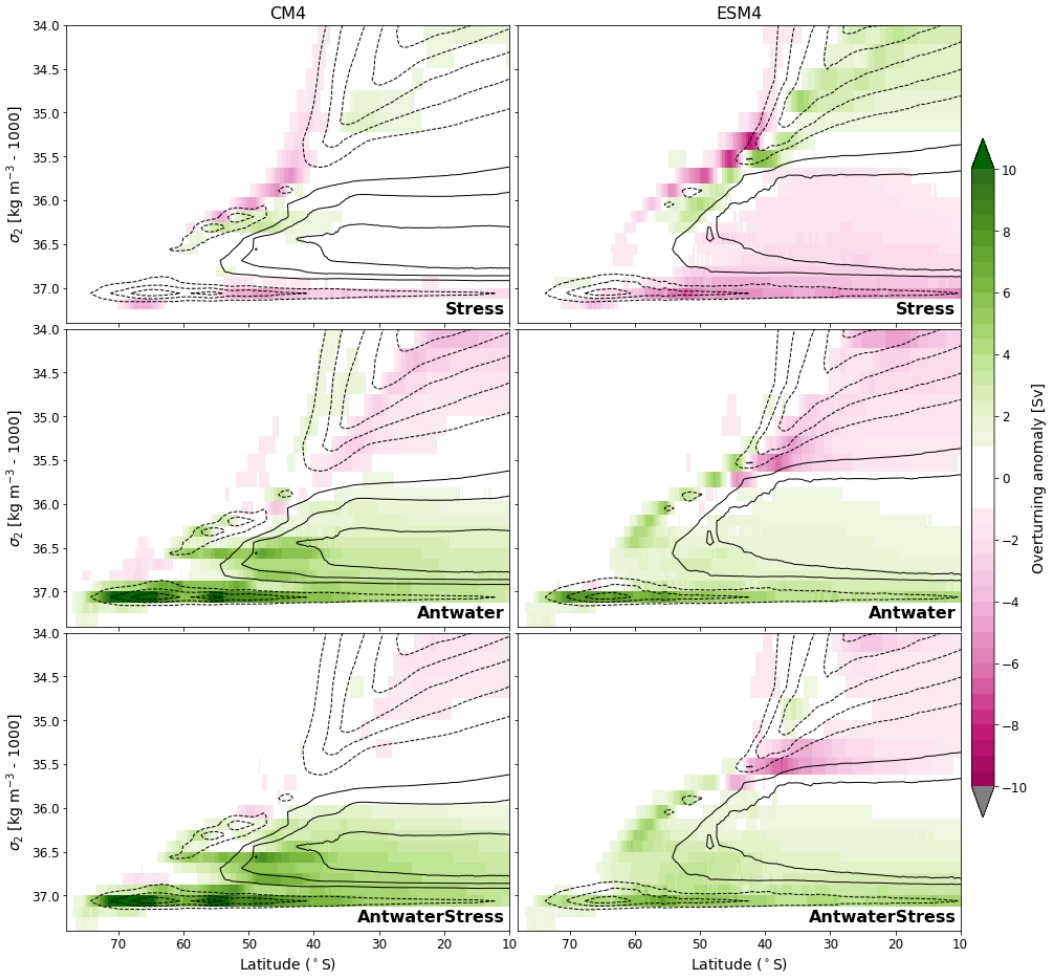

Figure 3. Anomaly in isopycnal overturning (Ψ) in CM4 (left) and ESM4 (right) in Stress (top row), Antwater (middle row) and AntwaterStress (bottom row). Anomalies are calculated from a 20-year mean (year 51-70) of each experiment minus the 100-year mean of the corresponding Control. The anomalies are given by the color shading, while the contours denote Ψ in the corresponding control run (100-yr mean) with intervals of 5 Sv.

The isopycnal overturning over the last 20 years of each perturbation is remapped to depth space along with the zonal mean density (Figure 4), which reveals substantial changes in the shape of the lower overturning in the experiments. In Stress, the overturning shape is roughly maintained, but with a pronounced lengthening towards lower latitudes. In response to the Antwater perturbation, the lower-limb overturning is almost completely shut off and confined to greater depths in CM4, while in ESM4, the circulation becomes shallower and more vertical. The strengthening of the bottom overturning in the Stress experiment is also accompanied by densification of the deep subpolar SO. In both CM4 and ESM4, enhanced and poleward shifted winds lead to an upward displacement of the 37.1 σ_2 isopycnal, which indicates more dense water production in response to the wind perturbation. Conversely, the increase in Antarctic melting causes a clear contraction of the isopycnal representing the upper bound of the bottom overturning cell (σ_2 = 37.0). The downward displacement of the 37.0 σ_2 isopycnal is about the same between CM4 and ESM4. However, in the subpolar latitude range (south of 60°S), there is more lightening apparent in CM4 compared to ESM4, which is in line with the stronger decline in the bottom overturning in CM4.

The analysis of the combined forcing of Antarctic meltwater and wind stress changes (AntwaterStress), reveals that freshening is the dominant effect, as the changes in Ψ seen in AntwaterStress are almost identical to those found in Antwater alone (Figure 3 and 4); the minimum (CM4: -11.4±0.6 Sv, ESM4: -14.1±1.8 Sv) and maximum of Ψ (CM4: 21.2±0.3 Sv, ESM4: 14.7±0.3 Sv) in AntwaterStress are very similar to those in Antwater. Given the stronger effect of wind stress on lower limb overturning in ESM4, one can detect the influence of this wind perturbation in the AntwaterStress of ESM4, mostly as a smaller reduction of the bottom cell compared to Antwater (Figures 3).

The impact of AIS melting and enhanced wind stress on the SO MOC are consistent with the meridional transport across 30°S (Table 2). The two models show comparable responses where AABW transport is reduced when Antarctic melting is included in the perturbation, while changes in wind stress alone leads to AABW export increases. Perturbations affect the deep waters flowing into the SO in the same manner as they impact the outflow of bottom waters, consistent with the notion of these two water masses constituting lower limb overturning. However, the change in volume transport is not as strong for the deep water masses (NADW, CDW) compared to the change seen in AABW outflow. Antwater (AntwaterStress) show reductions in bottom water outflow of -4.2 Sv (-4.8 Sv) and -3.7 Sv (-4.0 Sv) in CM4 and ESM4, respectively. On the other hand, the inflow of deep waters into the SO reduces only by 0.9 Sv (0.7 Sv) and 2.0 Sv (2.1 Sv), respectively. In the case of the Stress experiment, the AABW outflow increases by 2.8 and 4.8 Sv, which is comparable to the increases in CDW inflows by 3.0 Sv and 2.6 Sv in CM4 and ESM4, respectively.

The inflowing deep waters reduce not as much as the outflowing bottom water in Antwater and AntwaterStress. Presumably this is related to how the shape of the overturning changes, in which the inflow of NADW/CDW is maintained due to unchanged wind forcing, but the water mass transformation south of 30°S shifts to more lightening during subpolar freshening. This enhanced lightening of upwelled CDW is consistent with an overall increased outflow of intermediate water masses (AAIW/SAMW) from the SO (especially in the Atlantic basin) in the Antwater and AntwaterStress experiments (Table 2). Thus, enhanced freshening leads to a decline of the lower limb, associated with reduced northward AABW and southward NADW/CDW transport across 30°S, while the formation of lighter intermediate waters are increased, corresponding to a stronger AAIW/SAMW outflow and strengthening of the upper-cell.

It is notable that differences in the response to freshwater forcing between the two models are largely confined to the Southern Ocean (Figure 3). At 30°S, both models show broadly consistent changes both in magnitude and density distribution of the overturning (see Table 2). Observational estimates of the lower cell overturning strength and its

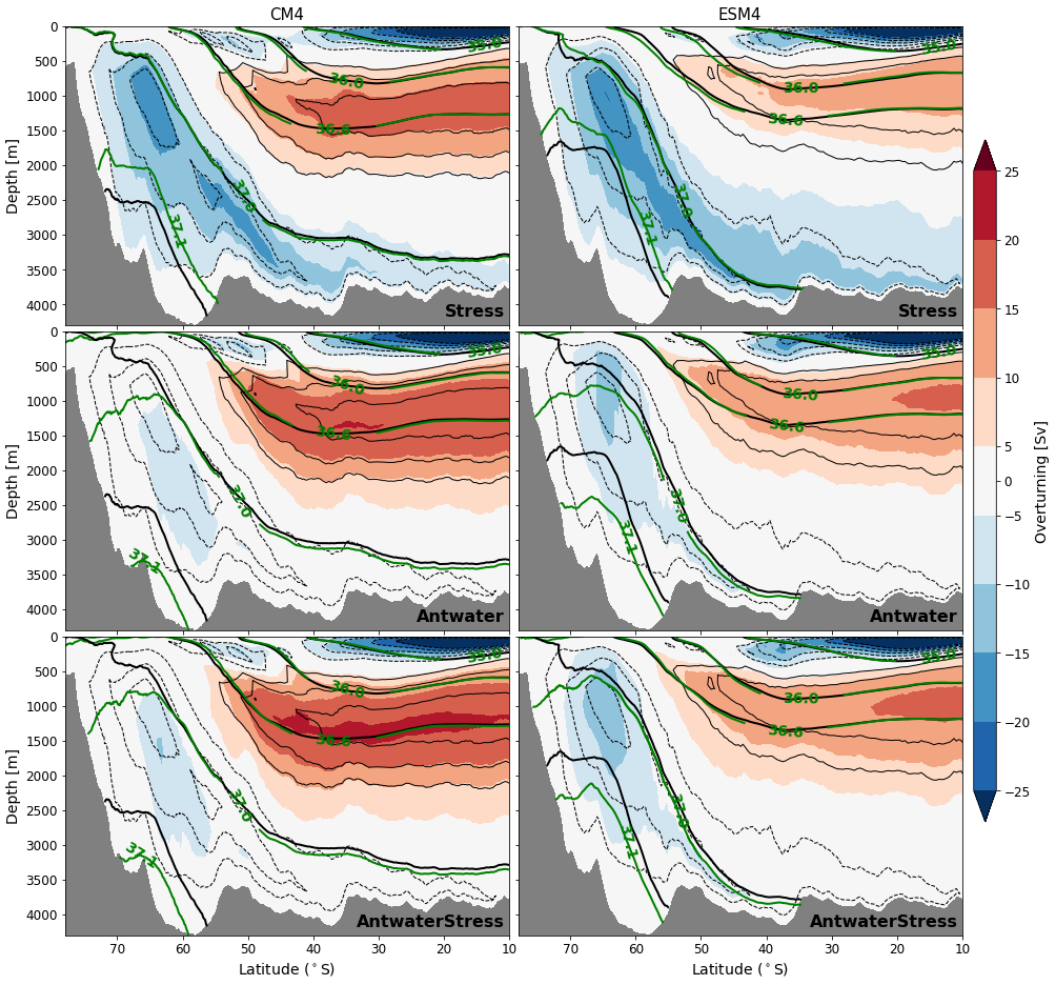

Figure 4. Isopycnal overturning reprojected to depth space for CM4 (left) and ESM4 (right). Colors represent the streamfunction of the 20-year mean in Stress (top), Antwater, (middle) and AntwaterStress (bottom), while the thin black contours denote the mean streamfunction of the 100-year period of the Control. Both filled and line contours are plotted with intervals of 5 Sv. The green contours denote the σ_2 isopycnals in the 20-year mean of the perturbation run, while the thicker solid black contours denote the σ_2 isopycnals in the 100-year mean Control period.

changes over time are commonly derived via inverse methods at the northern boundary of the Southern Ocean (e.g., Sloyan & Rintoul, 2001; Lumpkin & Speer, 2007; Talley et al., 2003; Talley, 2008). The possibility that substantively distinct responses of AABW and the overturning circulation within the Southern Ocean can give rise to the same change in overturning at its northern boundary, presents a challenge to interpretation of the lower cell response. Consequently, we turn our attention to the layer-wise mass budget at 30°S, making use of the WMT framework (Section 3.2) to decipher the balance of processes giving rise to the derived changes in each model.

3.2 Balance between water mass transformation, storage change and MOC at 30°S

The impact of both the wind and Antarctic meltwater perturbation are most pronounced in the lower cell of the SO MOC. The two perturbations have opposite effects,

Table 2. Change in meridional transport at 30°S in the perturbation experiments (Antwater, Stress and AntwaterStress) relative to the preindustrial control for CM4 and ESM4. Values are derived by taking the average of the last 20 years (year 51-70) of the ensemble mean minus a 100-year average of the corresponding control run. Percent change is only shown in the case where the standard deviation envelope does not include zero. Values in bold are absolute changes that correspond to more than 50% change compared to the control run and are outside of ±2 standard deviations. The transport changes are presented separately for the main water masses of the SO starting with the densest water mass (AABW). The values correspond to the same classes presented in Table 1, excluding TW and adding the changes for the intermediate water masses (AAIW & SAMW) together. CDW corresponds to NADW, PDW and IDW together.

	Antwater		Stress		AntwaterStress	
AABW	CM4	ESM4	CM4	ESM4	CM4	ESM4
Atlantic	**-1.3±0.3 Sv** (-51 %)	-0.6±0.1 Sv (-28 %)	+0.9±0.6 Sv (+35 %)	**+2.6±0.8 Sv** (+123 %)	**-1.6±0.4 Sv** (-63 %)	-0.9±0.1 Sv (-43 %)
Pacific	**-2.4±0.6 Sv** (-66 %)	**-2.8±0.3 Sv** (-60 %)	+1.7±0.7 Sv (+46 %)	+2.0±0.7 Sv (+43 %)	**-2.5±0.6 Sv** (-69 %)	**-2.8±0.4 Sv** (-59 %)
Indian	-0.5±0.2 Sv (-33 %)	-0.3±0.1 Sv (-25 %)	+0.3±0.6 Sv	+0.3±0.0 Sv (+22 %)	-0.7±0.1 Sv (-47 %)	-0.4±0.2 Sv (-32 %)
Total	**-4.2±0.7 Sv** (-55 %)	-3.7±0.3 Sv (-47 %)	+2.8±1.0 Sv (+37 %)	**+4.8±1.1 Sv** (+60 %)	**-4.8±0.7 Sv** (-63 %)	**-4.0±0.4 Sv** (-51 %)
CDW						
Atlantic	-0.1±0.5 Sv	+0.3±0.4 Sv	-0.9±0.3 Sv (+4 %)	-2.0±0.2 Sv (+10 %)	-0.6±0.2 Sv (+3 %)	-0.1±0.1 Sv
Pacific	+1.0±0.6 Sv (-40 %)	**+1.8±0.6 Sv** (-138 %)	**-1.8±0.5 Sv** (+76 %)	**-0.9±0.1 Sv** (+65 %)	+1.2±0.8 Sv (-49 %)	**+2.0±0.6 Sv** (-151 %)
Indian	0.0±0.3 Sv	-0.1±0.2 Sv	-0.2±0.4 Sv	+0.2±0.2 Sv	0.0±0.1 Sv	+0.2±0.2 Sv
Total	+0.9±0.9 Sv	+2.0±0.7 Sv (-10 %)	-3.0±0.8 Sv (+12 %)	-2.6±0.3 Sv (+13 %)	+0.7±0.8 Sv	+2.1±0.6 Sv (-10 %)
AAIW & SAMW						
Atlantic	+2.3±0.2 Sv (+18 %)	+1.6±0.6 Sv (+14 %)	0.0±0.6 Sv	-1.1±0.6 Sv (-9 %)	+2.7±0.3 Sv (+21 %)	+1.8±0.5 Sv (+16 %)
Pacific	+0.6±0.3 Sv (+9 %)	+1.2±0.2 Sv (+15 %)	+0.4±0.5 Sv	-0.3±0.5 Sv	+0.8±0.3 Sv (+13 %)	+1.5±0.8 Sv (+19 %)
Indian	**+1.3±0.3 Sv** (+117 %)	+1.0±0.9 Sv (+49 %)	0.0±0.2 Sv	-1.0±0.4 Sv (-50 %)	**+1.8±0.3 Sv** (+159 %)	+0.5±0.3 Sv (+23 %)
Total	+4.1±0.5 Sv (+23 %)	+3.8±1.1 Sv (+22 %)	+0.3±0.8 Sv	-2.5±0.9 Sv (-14 %)	+5.3±0.5 Sv (+30 %)	+3.8±1.0 Sv (+22 %)

manuscript submitted to *JGR: Oceans*

where enhanced and poleward shifted winds strengthen the lower cell whereas increased AIS melting weakens it. Contrasting the changes in the SO MOC seen in the Stress and Antwater experiments with the AntwaterStress experiment, it is clear that the increased melting from the AIS dominates the wind stress perturbation. To understand the impact of enhanced AIS melting on the lower limb MOC, it is necessary to evaluate the role of surface forcing and interior processes in the transient response. For this purpose, we apply the WMT framework (Figure 1) to compare changes in the surface and interior processes contributing to the circulation response that was observed in the previous Section. In this Section, we compare the balance between overturning at 30°S and processes integrated south of 30°S. Given the dominant role of AIS melting, we focus on the Antwater experiment relative to the Control in both CM4 and ESM4. Furthermore, since the changes are mostly seen in the lower limb circulation, we focus on the AABW and CDW density ranges ($\sigma_2 > 36.6$).

3.2.1 Mean-state representation

As described in Section 2.3 (and shown schematically in Figure 1), a volume balance in density coordinates is defined south of 30°S. Due to volume conservation, the change in volume below a given isopycnal (dV/dt) must equal the total WMT (G) across that isopycnal integrated south of 30°S and the overturning circulation along that isopycnal at 30°S (ψ) (see equation (1)). As noted in Section 2.3, G is decomposed into a surface (i.e, WMT due to surface buoyancy fluxes; G_{srf}) and interior term (i.e, WMT due to interior diapycnal fluxes; G_{int}), where the interior component is calculated from Equation (6). Figure 5a and b shows the balance of all these terms in σ_2 space, evaluated over the 100-year time means from the CM4 and ESM4 control experiments (see Section 2.2 for details of the chosen time periods). For a given σ_2 value, ψ is the volume transport at 30°S, the G terms represent volume flux across the isopycnal and dV/dt the storage change integrated over all denser layers. To further assist interpretation, Figure 5c,d show the discrete difference of these terms between density surfaces, which corresponds to their balance *within* each isopycnal layer. Note that the negative of ψ is plotted in Figure 5, so that the outflow of AABW at 30°S is positive.

Indicated by the similarity between the two model's overturning streamfunctions (Figure 2), ψ is very similar over the CDW and AABW density range (Figure 5a,b). The upper density bound of AABW varies slightly between CM4 and ESM4, but roughly lines up with the inflection points of ψ. In both models, the maximum in $-\psi$, which corresponds to the total export of AABW at 30°S, lines up with the CDW-AABW interface at $\sigma_2 \approx 37.05$. Looking at this density, representing the upper edge of the AABW, we can see that ψ arises mostly as a balance between G_{srf} and G_{int}. In CM4, there is a small negative tendency in dV/dt indicating a persistent model drift acting to deflate the bottom waters south of 30°S.

The two models show consistent patterns of G_{srf} in the CDW density range (Figure 5,c,d). Negative transformation of water lighter than ∼36.8 and positive transformation for denser water results in a divergence of water in this density range ($36.5 < \sigma_2 < 37.0$) – that is, overall destruction of this water mass due to surface forcing, as seen in the negative values of the ΔG_{srf} bars in panels c and d. In both models, interior mixing (G_{int}; green dashed line) acts to make water lighter in all density layers (seen as consistently negative values), except the very lightest layers in ESM4. Although the shape and magnitude of G_{int} varies between the models, its overall imprint in the CDW range – destroying water in the densest layers while forming water in lighter layers – is broadly consistent (green bars in panels c and d).

The shape of the overturning streamfunction (ψ) broadly matches that of the surface transformation (G_{srf}), implying that CDW brought southward at 30°S is mostly destroyed by surface forcing. The differential pattern of interior mixing across water masses

(G_{int}) acts to shift the inflowing water to a lighter density range prior to destruction at the surface (seen most clearly in Figure 5 c and d). It is notable that although the character of G_{srf} differs between models, *psi* is markedly similar in both shape and magnitude, indicating a compensatory balance between transformations due to surface forcing and interior mixing. An example is seen in the densest layers of CDW where ESM4 shows no destruction via surface forcing, with everything lost via mixing (Figure 5d), whereas both mixing and surface forcing balance the inflow in CM4 (with the remaining difference between the models explained by the transient storage). While it is true that, because G_{int} is inferred as a residual, it must be compensatory in some sense, our careful evaluation of the layer-wise balance shows that these differences between the models can *only* be explained by interior processes (see Methods, Section 2.3).

The positive G_{srf} at the high-end densities represents transformation to denser waters (i.e., densification) by surface buoyancy fluxes. Overall, G_{int} is negative over the relevant density range, which suggests that interior diapycnal mixing transforms waters to lighter density classes (i.e., lightening) and mostly compensates G_{srf}. With G_{srf} becoming subsequently smaller for $\sigma_2 > 37$, water is converging at the highest densities leading to surface-forced formation (Figure 5 c and d). In both models, we see that G_{int} removes any water masses denser than 37.2 and reduces and constrains the surface-formed AABW water mass to a narrower density range (σ_2 = 37.1-37.2), which is the densest water exported at 30°S (Figure 2). Furthermore, as in the CDW range described above, any differences in G_{srf} between the two models are accommodated by the same differences in G_{int}. For example, the greater values of G_{srf} at $\sigma_2 = 37.0$ in CM4 (12.3 Sv versus 9.4 Sv in ESM4) is accompanied by a greater compensation by G_{int}, such that total ψ is roughly 8 Sv for both. Thus, in CM4 more surface-forced dense water is destroyed by lightening through mixing processes as compared to ESM4.

The black dotted and dashed line in Figure 5a,b denote the thermal (i.e., surface heating and cooling) and haline (i.e., surface freshening and salinification) contributions to G_{srf}, respectively. From this decomposition it is clear that surface densification is primarily driven by the haline term, which in turn arises mainly from brine-rejection during sea ice formation over the Antarctic shelf (grey dash-dotted line). This process is consistent with previous studies using numerical models (e.g., Moorman et al., 2020), ocean reanalysis (Abernathey et al., 2016) and observation-based estimates (Pellichero et al., 2018). At the highest densities, G_{srf} in both models agree, with CM4 showing a greater maximum centered at a slightly higher density than ESM4. This difference in total WMT comes from the greater transformation in the haline component, because at this density range the net impact of surface forcing is densification due to brine rejection. Thus, the impact of sea ice formation in the surface WMT is slightly greater in CM4 compared to ESM4.

The fact that dV/dt is small in absolute terms confirms that the models are in a quasi-steady state in the control run, where changes in the volume of any density layer are negligible over the long term (100 years). The only exception to a true steady state is at the boundary between AABW and CDW, where we see a nonzero trend in volume. This trend reflects the long-term (centennial to millennial) drifts in bottom waters commonly seen in coupled climate models (Gupta et al., 2013; Irving et al., 2021). The drift is stronger in CM4, where dV/dt is -2.9 Sv at $\sigma_2 = 37.05$, compared to -1.4 Sv at $\sigma_2 =$ 36.95 in ESM4. In both models, the drift is constrained to the upper bound of the AABW, which suggests potential bias in bottom waters over centennial scales. Nonetheless, dV/dt is much smaller (within 5%) compared to the values associated with the other terms, such that $-\psi \approx G_{srf} + G_{int}$. A discussion of the causes of the drift are beyond the scope of this analysis, but are likely related to an imbalance between surface formation and interior consumption of dense bottom waters (Adcroft et al., 2019; Dufour et al., 2017; Lee et al., 2002).

In summary, this layer-wise budget of the deep and bottom waters reveals that although the shape and magnitude of ψ is consistent between the models, the contributing mechanisms are distinct. In particular, G_{srf} contributes approximately similarly to the outflowing AABW between the two models. However, there is a much more substantial net contribution from G_{int} in ESM4, but minimal contribution in CM4. Furthermore, these differences arise via distinct patterns in transformation, whereby the contribution in ESM4 arises from an absence of interior transformation at the upper isopycnal boundary, while the negligible net formation in CM4 is due to an approximate balance between negative transformations at both the lower and upper bounds of the AABW. Additionally, it is worth noting the distinct nature of the balance between G_{srf} and G_{int} in the density layer just denser than outflowing AABW. Despite the terms balancing exactly in both models, leading to zero net outflow of water in this density layer at 30°S, the magnitude of the individual terms is roughly four times larger in CM4 than ESM4. These processes relating to the formation of outflowing AABW will prove crucial in interpreting the transient response of this water mass to surface forcing changes, with a key detail being the overall greater *throughflow* of water (seen in the magnitude of the mixing term) in CM4 relative to ESM4 at steady-state.

3.2.2 Transient response

We now assess how the layer volume balance between the isopycnal overturning at 30°S and WMT south of 30°S changes in the Antwater perturbation experiments. We consider this both by comparing a 20-year mean in the perturbation experiments (Figure 6, solid lines) to the 100-year mean steady-state balance (Figure 5, and faded lines in Figure 6), and by looking at the full evolution of the terms over time (Figure 7). As seen in Figure 3, in both CM4 and ESM4, the lower limb overturning weakens in response to the increased Antarctic melting. By comparing the 100-year mean steady-state balance of the control runs (as presented in Figure 5 and redrawn in faded colors in each panel of Figure 6) with the mean balance over the last 20 years (years 51-70) of the perturbation experiments, net export reduces by 4 Sv within the AABW density range in both models (Figure 6 and Table 2). The temporal evolution of change in $-\psi$ during the Antwater perturbation run is presented as a Hovmöller diagrams (Figure 7a, b) showing the anomaly from the 100-year mean of the control run in density space for each year (annual mean). The anomalies in $-\psi$ related to the AABW weakening start to develop around 20 years into the perturbation run and gradually increase in magnitude, such that the AABW export at 30°S steadily weakens during the simulation.

While the response in ψ is similar between the two models, the contributing mechanisms are markedly distinct (Figure 6). In particular, in spite of the models experiencing the same surface forcing change, the response in G_{srf} differs substantially (black lines and bars in Figure 6). Negative anomalies in G_{srf} in the last 20 years of the perturbation are mostly due to a shift in transformation towards lighter densities. The decline in G_{srf} is more pronounced in CM4, leading to a substantial weakening in total transformation (by $\sim$5 Sv) over both the AABW and CDW density range compared to the Control. In the case of ESM4, the shift towards lighter densities is smaller with a reduction in G_{srf} only apparent in the AABW density range (by 2-3 Sv) (Figure 6). The negative anomalies in G_{srf} establish within the first 10 years and remain fairly constant throughout the rest of run (Figure 7). Thus, there is an apparent lag of $\sim$10 years between a relatively fast adjustment of G_{srf} and the initiation of a more gradual decline in ψ at 30°S. This response in ψ is similar between CM4 and ESM4, even though we see characteristically different changes in G_{srf} between the two models.

The most striking difference in the model response is that of dV/dt (blue lines and bars in Figure 6; panel e and f in Figure 7). Crucially, this difference emerges in the outflowing AABW range, wherein the net deflation of the AABW volume is occurring roughly four times faster in CM4 than in ESM4. The formation perspective shows that, in both

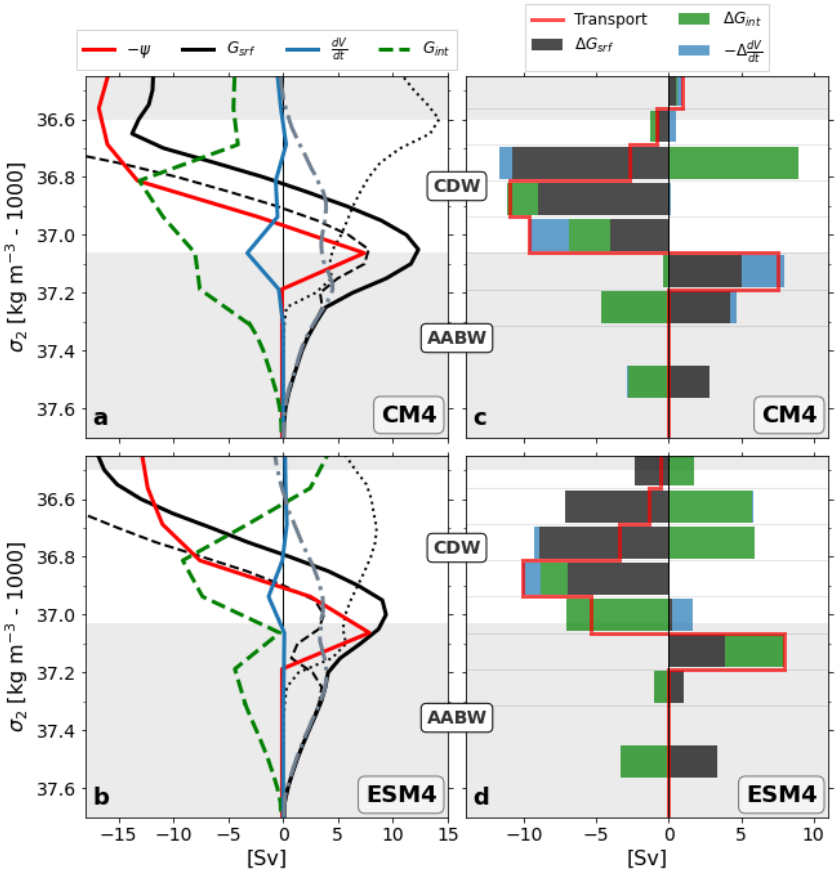

Figure 5. (a,b) Isopycnal overturning at 30°S ($-\psi$, red), plotted along with the total surface-forced WMT (G_{srf}, black), storage change (dV/dt, blue) and inferred interior WMT (G_{int}, green) south of 30°S, estimated in (a) CM4 and (b) ESM4. G_{srf} is further decomposed into its thermal (dotted) and haline component (dashed). Surface WMT occurring over the Antarctic shelf is represented by the grey dash-dotted line. Positive transformation corresponds to transport towards denser water classes and negative transformation to lighter water classes. dV/dt represents the total volume change below the isopycnal of the corresponding σ_2 value. ψ represents total export (positive) or import (negative) below the isopycnal of the corresponding σ_2 value. In panels (c, d) the export/import at 30°S (red line) are compared to formation/destruction from surface (black bars) and interior WMT (green bars) and storage change (blue bars) at discrete density bins as positive/negative quantities. Quantities in (c,d) are calculated as the negative difference from the corresponding terms in (a,b). The lightly shaded band in the lower half of the two panels identify the density range of the AABW, while the non-shaded band represents the density range of the CDW.

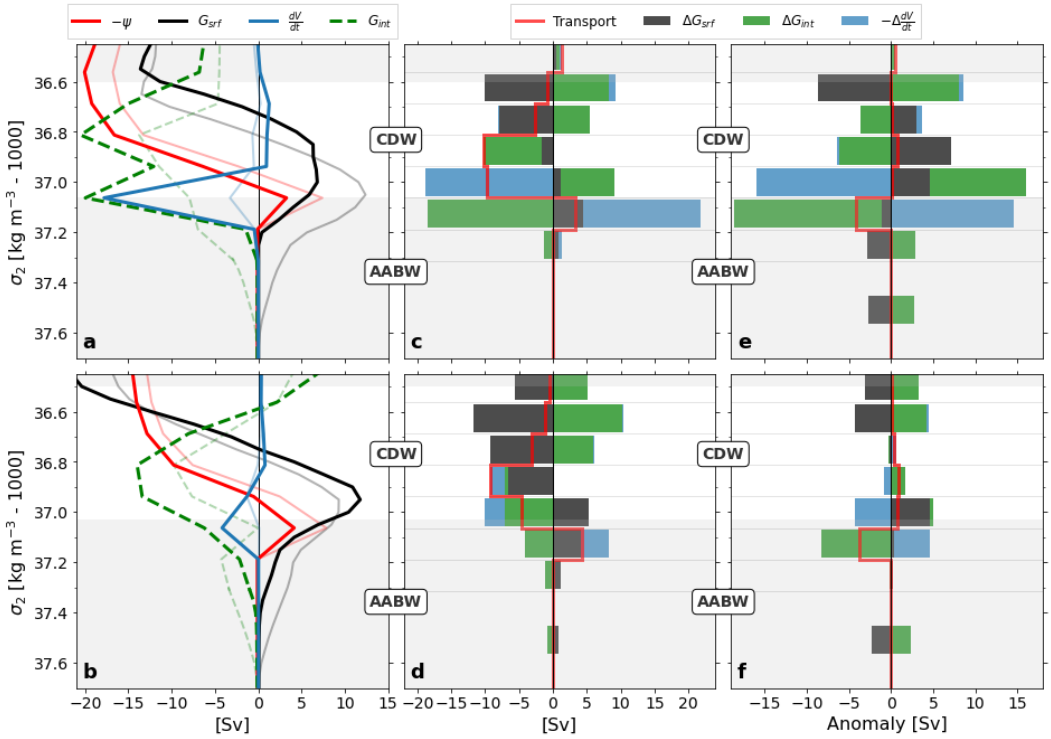

Figure 6. (a,b) Same as Figure 5 a and b, but including the mean of the last 20 years of the Antwater experiment (year 51-70) as highlighted curves. The curves for the 100-year mean of the control runs (as presented in Figure 5) are shown in lighter hue for reference.(c,d) Same as Figure 5 c and d, but for the last 20 years of the Antwater experiment (year 51-70). (e,f) Anomalies in the export/import at 30°S (red line), formation/destruction from surface (black bars) and interior WMT (green bars) and storage change (blue bars). Anomalies are calculated from the mean of the last 20 years (year 51-70) in Antwater minus the 100-year mean of the corresponding Control.

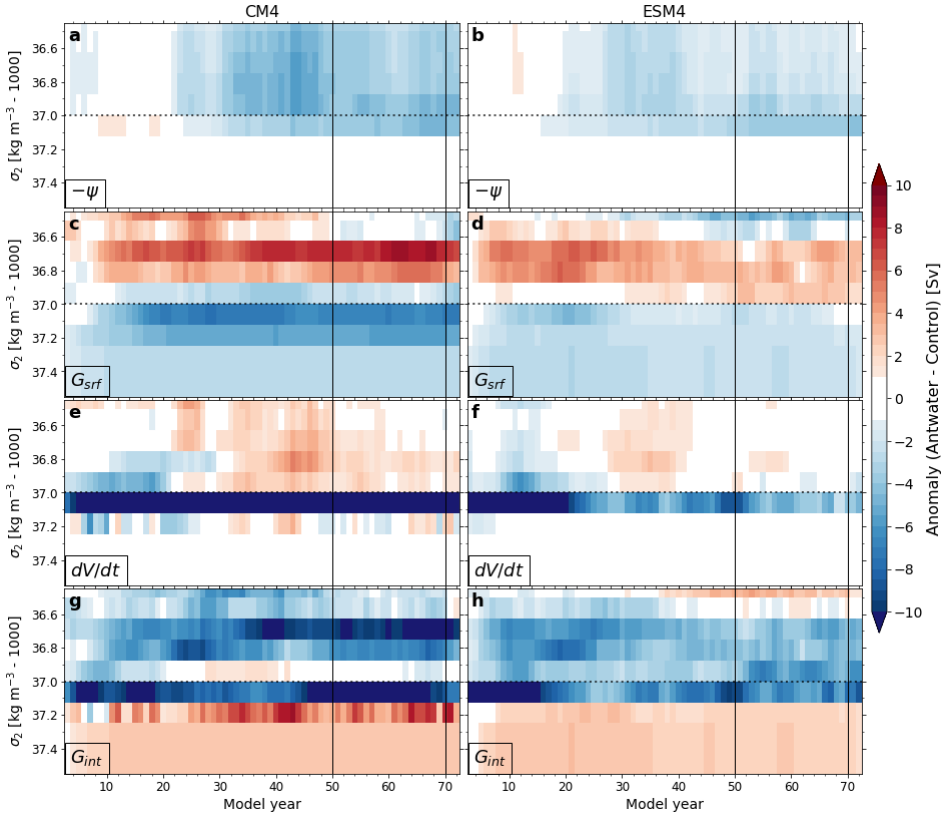

Figure 7. Hovmoeller-type diagrams of annual anomalies in (a,b) $-\psi$, (c,d) G_{srf}, (e,f) dV/dt and (g,h) G_{int} in the Antwater experiment relative to the 100-year mean of the Control run. Anomaly time series are presented in discrete density bins corresponding to the density levels of the model's diagnostic output. A 5-yr running mean is applied across each density class. The vertical lines indicate the 20-year averaging period at the end of the experiment used for Figure 6. The dotted horizontal line at $\sigma_2 = 37.05$ denotes the boundary between AABW and CDW.

models, the volume lost from AABW is going in the density class directly above (Figure 6 e,f). The transient perspective (Figure 7) reveals that the response of the models are similar over the first ∼20 years following the onset of the perturbation, with AABW deflating at a rate exceeding 10 Sv. However, whereas the anomaly persists over the subsequent 50 years in CM4, it is substantially reduced in ESM4.

The non-zero storage term is consistent with models still being in a transient state 70 years after the perturbation is imposed. The deviations from the steady state are mostly constrained to the isopycnal representing the boundary between the CDW and AABW and is characterized by a drift in AABW volume towards the overlying CDW. Away from the CDW-AABW interface, the storage change is close to zero for years 50-70 of the Antwater experiment (Figure 6). An open question is whether the deflation of AABW will eventually stop, providing a timescale of adjustment to the AIS meltwater perturbation for each model, or AABW outflow at 30°S to cease before a new steady state is reached. To answer this question would require much longer simulations, which was not feasible with global coupled climate models.

Over the last 20 years of the Antwater simulation, CM4 still experiences a loss of ∼20 Sv in dense AABW to the lighter CDW, which is much larger than the corresponding export at 30°S ($\psi = 3$ Sv). On the other hand, dV/dt over the last 20 years in the Antwater simulation with ESM4 is only -5 Sv, such that the response in dV/dt clearly differs between CM4 and ESM4. Given the comparatively modest and consistent evolution of the other, directly-evaluated budget terms (G_{srf} and ψ), the distinct model response in dV/dt can only be explained by model differences in interior transformation (G_{int}). The model differences in dV/dt are linked to distinct changes in G_{int}, where stronger lightening of AABW in the interior are inferred in the case of CM4 compared to ESM4 (Figure 6a,b). Furthermore, the variation of dV/dt at the CDW-AABW interface ($\sigma_2 \approx 37.0$) corresponds to variations of G_{int} (Figure 7g,h).

Looking more closely at the form of the inferred changes in G_{int}, we can identify further distinctions in the models' responses. The changes in both models is characterized by a decline in the transformation of outflowing AABW at its denser isopycnal bound ($\sigma_2 \approx 37.2$) and an increase in transformation at its lighter isopycnal bound ($\sigma_2 \approx 37.0$, see green dashed lines in Figure 6a,b). Notably however, the changes are much larger in CM4 than ESM4. In CM4, lightening of water at the upper density bound of outflowing AABW almost entirely shuts off, dropping from ∼10 Sv to ∼1 Sv (green dashed line at $\sigma_2 = 37.2$ in Figure 6a). In ESM4, a similar decrease takes place, but transformation is not shut off completely (reduced from ∼5 Sv to ∼3 Sv). At the lighter density bound, transformation doubles in CM4, from ∼10 Sv to ∼20 Sv. In ESM4, transformation at the lighter bound is initially zero, and increases to ∼8 Sv.

Revisiting our perspective on the formation of outflowing AABW in the time-mean state (Section 3.2.1), Figure 6 indicates that the supply of the water mass at the denser bound has been diminished, while its removal at the lighter bound has been increased. Crucially, the magnitude of these changes at both upper and lower bounds is much more pronounced in CM4 than ESM4. This diverging response of interior transformations at the upper and lower density bounds of the AABW ultimately accounts for the large differences in the deflation of AABW between the models. To derive further insight on the mechanisms leading to the different model responses in volume storage, we consider their spatial pattern.

The anomalies in dV/dt at $\sigma_2 = 37.05$ (corresponding to the upper density bound of AABW) over the last 20 years of the Antwater experiment are mapped in Figure 8 to see the geographic distribution of the AABW deflation. The overall negative anomalies of dV/dt at $\sigma_2 = 37.05$ reveal strong volume losses in CM4 that are constrained to the deep ocean basins of the Weddell and Ross Seas. The dV/dt anomaly pattern in ESM4 is also constrained to depths > 4000 m, but has generally weaker negative values and,

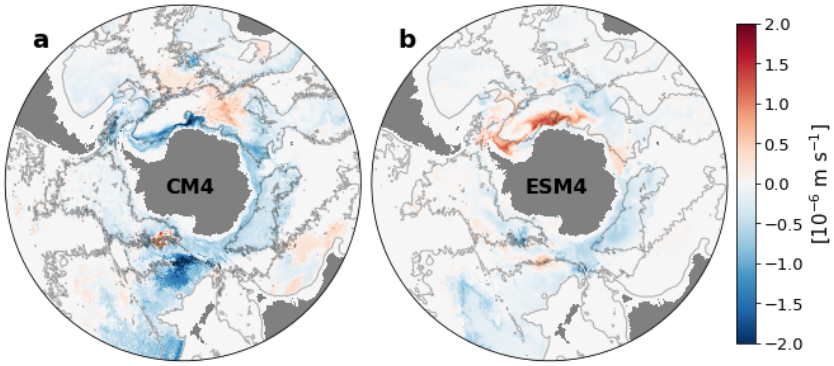

Figure 8. Spatial distribution of dV/dt anomalies evaluated at the upper density bound of the AABW ($\sigma_2 = 37.05$) in (a) CM4 and (b) ESM4. The anomalies are calculated from the average over the years 51-70 of the Antwater experiment minus the 100-year average of the Control. Note that dV/dt is divided by the horizontal area of a grid cell to render units of m s^{-1}. The light gray lines denote contours of bottom topography (4000-m isobath).

more importantly, includes regions of positive dV/dt anomalies in the Weddell Sea. This suggests dense bottom water still forming off the Weddell shelf in ESM4, but not in CM4. This large difference in the changes in isopycnal volume drift between the models is not reflected in changes in ψ, which are the same for the two models (Figure 6). Instead, the different response in dV/dt between the models must lie in the changing balance between G_{srf} and G_{int}.

Given that the meltwater perturbations are imposed at the surface and not in the interior, the forced changes in the perturbed state that are driving variability in G_{int} and dV/dt must be represented by anomalies in G_{srf}. Thus, the model-dependent response in G_{srf} determines corresponding changes in G_{int}, which in turn lead to changes in dV/dt. The decline in G_{srf} over the high-end densities impacts G_{int} in the density range that corresponds to AABW at 30°S. This adds to a deflation of AABW, seen as more negative dV/dt at the upper density bound of AABW, and is four times stronger in CM4 compared to ESM4.

3.3 Changes in the surface WMT on the Antarctic shelf versus open ocean

In this section we test whether the stronger deflation of AABW in CM4 is related to the overall greater decline of G_{srf} over the AABW density range ($\sigma_2 > 37.0$). Mapping the anomalies in G_{srf} from the last 20 years of the Antwater experiment for the upper density bound of AABW ($\sigma_2 = 37.05$) shows that the decline in surface transformation occurs mostly on the Antarctic shelf (Figure 9). The reduction in G_{srf} is weaker in ESM4 and, unlike CM4, the negative anomalies are not present in most DSW formation regions, such as the Weddell and Ross shelves. This distinction suggests that DSW formation and overflows are still present in the last 20 years of the simulations in ESM4, which explains the smaller drift in the AABW volume. For both models, G_{srf} anomalies are comprised mostly by the haline component (Figure 9, right column) with much smaller changes in the thermal component (Figure 9, middle column). This result suggests that the largest impact of Antarctic melting is a decline in haline driven formation of DSW. This reduction in DSW formation is much more apparent in CM4 than in ESM4.

To better quantify the reduction of G_{srf} on the Antarctic shelf, we repeat the calculation in Equation (4) south of 60°S and differentiate between surface-driven transformation on the shelf and offshore (Figure 10). Furthermore, we isolate surface trans-

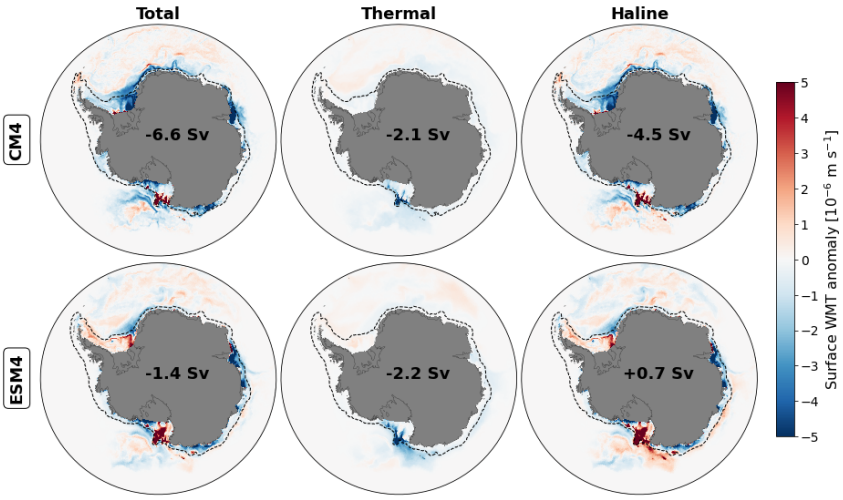

Figure 9. Spatial distribution of G_{srf} anomalies evaluated at the upper density bound of the AABW ($\sigma_2 = 37.05$) in CM4 (top) and ESM4 (bottom). The anomalies are calculated from the average over the years 51-70 of the Antwater experiment minus the 100-year average of the Control. Total anomalies (left) are compared to anomalies in the thermal (middle) and haline component (right). The area-integrated change in G_{srf} is printed in the center of each map and corresponds to the difference between Control and Antwater in Figure 6. The 1000-m isobath is shown as black dashed contours which delineates the Antarctic shelf from the open ocean.

formation due to freshwater and salt fluxes since it has been established that those are driving the changes in G_{srf}. We define the Antarctic shelf as the region shoreward of the 1000-meter isobath around Antarctica, while the open ocean region is offshore from the 1000-meter isobath and south of 60°S. DSW formation due to brine rejection is defined as the maximum transformation over the Antarctic shelf in the Control experiment, which occurs at $\sigma_2 = 37.19$ in CM4 and $\sigma_2 = 37.25$ in ESM4 (Figure 10). Based on the 100-year mean Control experiment, DSW formation is 4.5 Sv and 4.0 Sv in CM4 and ESM4, respectively, which is dominantly driven by brine rejection from sea ice formation. Comparing this formation to the mean of the last 20 years (51-70) of the Antwater experiment, DSW formation nearly ceases in CM4 while only reducing by about 50% in ESM4. The different response between CM4 and ESM4 in terms of DSW is true for both Antwater and AntwaterStress.

Besides the changes occurring on the shelf, the two models also show different responses in the open ocean. In ESM4, the increases in surface WMT to denser water classes are contrasted with a clear decline in surface WMT found in CM4. The increased surface WMT in the open ocean is linked to increased brine rejection due to sea ice growth. This result is consistent with findings by Beadling et al. (2022), who showed sea ice thickening in the Ross Sea and Weddell Sea in response to Antarctic melting. The sea ice expansion and thickening are greater in ESM4 compared to CM4, and are reduced in the combined AntwaterStress experiment. This result points to potentially important impacts on open ocean ventilation related to Antarctic meltwater. However, the offshore surface transformation occurs at densities that are not high enough to affect the AABW. In the case of both the Control steady (Figure 5) and Antwater transient state (Figure 6), any changes in surface densification in the open ocean happen at density classes that show lightening by interior processes. Thus, any water masses that form in this density range ($\sigma_2 \leq 37.1$) will not reach densities relevant for AABW volume and export at 30°S.

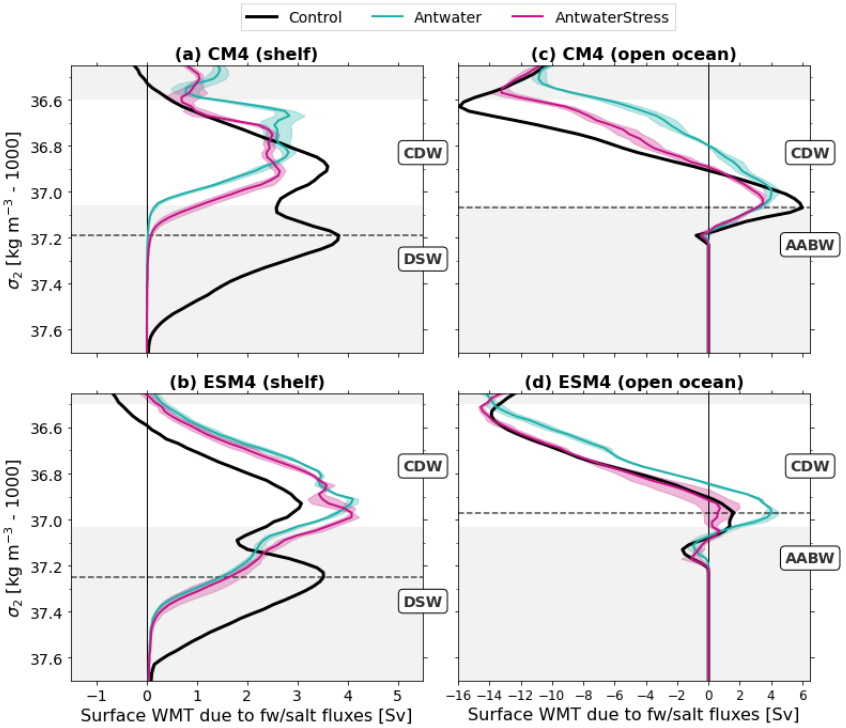

Figure 10. Surface-forced WMT south of 60°S decomposed by transformation occurring over the Antarctic shelf (left column) and over the open ocean (right column) for CM4 (top row) and ESM4 (bottom row). Black lines represent the 100-year mean from the corresponding Control run, while the colored lines represent the 20-year mean of Antwater (cyan) and AntwaterStress (magenta). WMT is presented in σ_2-space with density bins of 0.02 kg m−3. Positive values corresponds to transport towards denser water classes and negative transformation to lighter water classes. The 20-year mean WMT curves for Antwater and AntwaterStress include ±1 standard deviation envelope based on the ensemble.

3.4 Sensitivity of the transient response of DSW formation to ASC representation

Differentiation of G_{srf} between Antarctic shelf and offshore (Figure 10) shows that any surface formation of DSW ($\sigma_2 > 37.2$) occurs over the Antarctic shelf. The AABW exported at 30°S is associated with lighter densities of $37.0 < \sigma_2 < 37.1$ (Figure 5). Hence, the waters formed on the shelf are being made considerably lighter by interior mixing processes before being exported northward at 30°S, such that DSW and AABW masses cannot be directly linked in density space. The layer-wise volume budget in the steady state of both CM4 and ESM4 shows that mixing leads to destruction of water denser than $\sigma_2 > 37.2$ (Figure 5). Due to volume conservation, this destruction must contribute to the formation of AABW at a lighter density layer ($37.1 < \sigma_2 < 37.2$). Thus, G_{int} redistributes the densest water formed at the Antarctic shelf to a lighter and more narrow AABW density class. An important consequence from the balance between G_{srf} and G_{int} is that DSW needs to be formed at densities greater than what is found in the deep SO.

Accounting for the role of interior mixing, DSW contributes about half to the AABW export at 30°S in both CM4 (4.5 Sv of DSW formation compared to 7.5 Sv of AABW export at 30°S) and ESM4 (4.0 Sv of DSW formation compared to 8.0 Sv of AABW export at 30°S) in the Control state. This contribution suggests that stability of the AABW depends on the production of DSW occurring over the high-end density range ($\sigma_2 > 37.2$). This budget is schematically represented in Figure 11a, which illustrates the steady-state balance between G_{srf}, G_{int} and $-\psi$. In this case, the AABW volume (defined below the isopycnal surface $\sigma_2 = 37.05$) remains constant, such that dense water formation occurring at $\sigma_2 \geq 37.05$ (occurring both on the shelf and in the open ocean) is balanced by lightening due to diapycnal mixing and the transport at 30°S. This quasi-steady state volume balance applies to the Control in both models, with the exception that CM4 includes a small drift in AABW volume (negative dV/dt at $\sigma_2 = 37.05$).

The Antwater perturbation, representing increased melting of the AIS, results in characteristically different responses between the two models (Figure 11 b and c). By focusing on the Antarctic shelf, we identified the response of DSW to the AIS melting as a key difference between CM4 and ESM4. This distinct response is connected to how the Antarctic Slope Front and associated ASC are resolved in the two models. In particular, it has been demonstrated that the ASC is stronger and more refined in CM4 than ESM4 Beadling et al. (2022) in the model's mean state, primarily due to finer horizontal grid spacing in CM4 (0.25°) compared to ESM4 (0.5°). (Beadling et al., 2022) showed that in response to the Antwater perturbation, the stronger mean-state ASC in CM4 traps more freshwater along the Antarctic shelf, leading to a strong acceleration of the ASC, and additional freshwater trapping, as the density gradient increases between the shelf and open ocean. This freshwater trapping mechanism identified in Beadling et al. (2022) in CM4 leads to a more regionally confined freshening of the Antarctic shelf in the Antwater experiment, shutting off DSW formation (Figure 10). Since there is no more overflow of DSW supplying the deep SO, the AABW volume declines, as reflected by a slumping of the isopycnal surface corresponding to $\sigma_2 = 37.05$ (Figure 11b).

Given the less refined ASC, the density gradient between shelf and open ocean does not sharpen as much in ESM4 in the Antwater experiment. There is more cross-shelf export of meltwater away from the shelf, leading to an attenuated freshening of the shelf. The advection of freshwater away from the shelf and lack of a trapping mechanism explains why DSW formation is only reduced by about 50% in ESM4 rather than being shut off (Figure 10), such that dense overflows are still present in ESM4's Antwater experiment. Based on spatial anomalies of the AABW storage change (Figure 8) these overflows occur mostly from the Weddell shelf. The continued presence of DSW formation and overflows in ESM4's Antwater and AntwaterStress simulations explains why there is less volume reduction in ESM4's AABW layer compared with CM4 (Figure 11c).

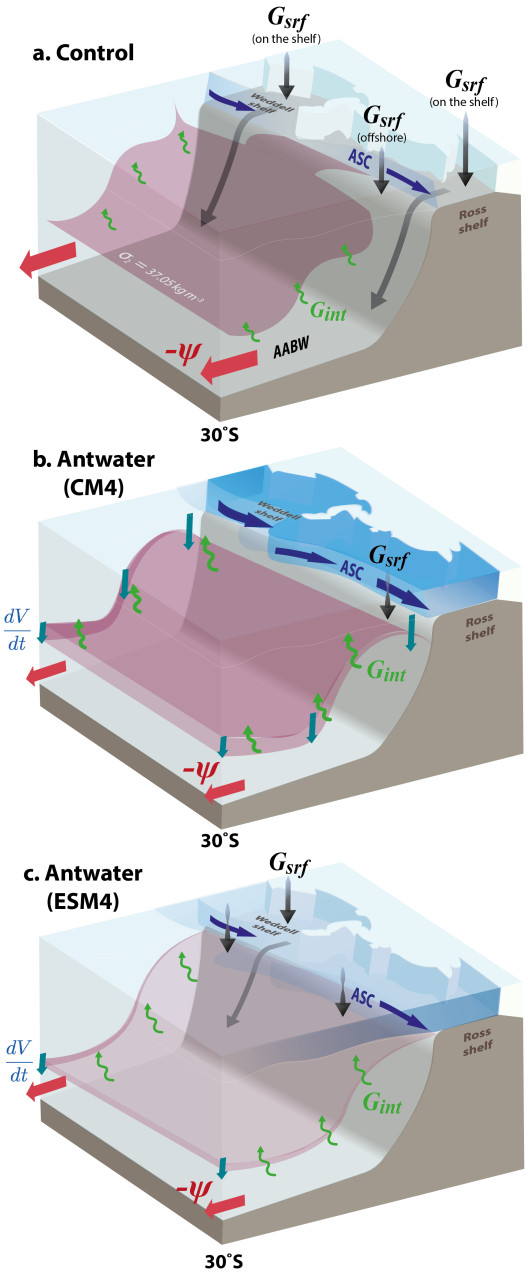

Figure 11. Schematic of processes associated with the AABW volume balance in the SO (south of 30°S) based on the Control run in both CM4 and ESM4 (a) and the Antwater experiment in CM4 (b) and ESM4 (c). The isopycnal surface for $\sigma_2 = 37.05$ is shown in purple shading and denotes the upper (lighter) bound of the AABW. Red arrows denote the AABW export quantified as $-\Psi$ at 30°S and $\sigma_2 = 37.05$. The downward pointing arrows in black denote positive surface WMT for $\sigma_2 \geq 37.05$ occurring both in the open ocean and on the Antarctic shelf and cause dense water formation within and into the AABW layer. The upward pointing green arrows represent negative interior WMT at $\sigma_2 = 37.05$ and cause lightening of AABW water into the overlaying CDW water mass. The downward sloping arrows denote dense shelf water transforming into AABW. The dark blue arrow denotes the ASC. Thicker arrows in Antwater(CM4) indicate a stronger ASC compared to Control and Antwater(ESM4). The downward pointing blue arrows in Antwater(CM4) and Antwater(ESM4) illustrate the deflation of the AABW volume.

As explained above, the extent of AABW deflation is governed by surface WMT changes over the Antarctic shelf. Changes in surface WMT over the open ocean indicates no effect on the AABW (Figure 10). Any surface densification in the AABW density range that occurs over the open ocean is opposed by interior lightening in the Antwater experiment. This two-way balance between surface and interior processes is illustrated in Figure 11 b and c, showing G_{srf} directly compensated by G_{int} over the open ocean. This compensation is consistent with the findings that the additional meltwater input from the AIS equally suppresses open-ocean deep convective events in both models (Beadling et al., 2022). This result suggests that the impact in eliminating surface-forced dense water formation over the open ocean is the same in the two models. Thus, changes in open ocean surface WMT do not explain the stronger decline of AABW volume in CM4 relative to ESM4.

Despite the clear differences seen in the AABW volume change between the two models, the reduction in overturning at 30°S is roughly the same. Considering the balance described in Equation (1), the change in G_{int} must differ between the models in order to compensate for the differences in dV/dt and G_{srf} changes, such that $-\psi$ is responding the same way in the two models. Similarly, given the extent to which AIS melt perturbs dense water formation on the shelf, our analysis suggests that relevant mixing processes in the interior respond differently. In CM4, the complete elimination of DSW overflowing to the deep ocean leads to strong destruction of AABW by diapycnal mixing processes, which drives the deflation of the AABW. This behavior is not seen in ESM4, where there is only a moderate deflation of AABW that is likely driven by ongoing volume export at 30°S while any surface densification in the AABW density range is exactly balanced by destruction due to interior WMT. Thus, in addition to the representation of the Antarctic shelf processes, our analysis suggests potentially important differences in the representation of interior mixing processes between the two models.

4 Discussion

4.1 Impact of wind stress and Antarctic melting changes on SO water masses

In this study, we investigated the transient response of the SO MOC to changes in wind stress and AIS melting in GFDL's current-generation coupled climate models, CM4 and ESM4. These models are part of the CMIP6 suite and are widely used to study historical and future climate change. Due to its immense capacity to store heat and carbon, the deep SO has a significant influence on the global climate. Therefore it is critical to assess the response of deep SO circulation and water masses in these models to better understand their projections of future climate. To test the response of CM4 and ESM4, we designed idealized perturbations that represent expected changes in wind stress and AIS melting by mid-21st century in a high CO_2 emission scenario (i.e., RCP8.5 or SSP5-8.5 scenarios). These simulations allowed us to attribute the transient responses to the individual and combined changes from the forcings deemed most relevant for the SO.

In terms of the SO MOC, both perturbations yield the largest impact on the lower limb circulation cell, corresponding to CDW and AABW. Projected wind stress changes increase bottom water formation and enhance CDW inflow, while projected increases in AIS melting cause a substantially weaker bottom overturning cell and contraction of the AABW volume. A pronounced AABW and lower limb MOC with stronger and/or southward-shifted westerlies have been previously documented in both coupled and ocean-only models using different experimental designs (Bishop et al., 2016; Dias et al., 2021; Hogg et al., 2017; Spence, Sebille, et al., 2014). The simulated change in CM4 and ESM4 agree with these previous findings. However, we see interesting differences in terms of the sensitivity of the MOC to wind stress changes, where the lower resolution model ESM4 shows

a more enhanced bottom cell compared to the higher resolution model CM4. In both models, the lower cell is enhanced due to open-ocean polynyas that lead to strong heat losses and deep convection events (Beadling et al., 2022).

The higher sensitivity of changes in wind forcing in ESM4 is linked to a larger role of these open-ocean convection events, which occur quasi-periodically on a centennial time scale in the Ross Sea and Weddell Sea over the Control simulation (Dunne et al., 2020; Beadling et al., 2022). In ESM4, such polynyas develop early on in each ensemble member of the Stress experiment, which leads to substantial AABW production. On the other hand, the response in CM4 to wind perturbations is muted relative to ESM4, where the occurrence of open-ocean deep convection during Stress depends on the amount of heat stored within the CDW at the time of the perturbation initiation (Beadling et al., 2022). The dominance of open-ocean convection in response to wind perturbation has been observed in other climate models, such as ACCESS-OM2 (Dias et al., 2021), but are regarded as unrealistic given that most of AABW in the present day is sourced from DSW on the Antarctic shelf and not in the open ocean (Heuzé, 2021; Akhoudas et al., 2021). However, it is possible that open ocean convection may have been an important process in maintaining lower-limb overturning under the preindustrial climate, and the weaker AABW production during current climate condition is due to the absence of such phenomena in the SO (C. d. de Lavergne et al., 2014).

With regard to a pure wind forcing scheme, we agree with the assessment of Dias et al. (2021) that coarser models such as ESM4 might be overly convective, such that they are too sensitive to projected wind changes, eradicating potential impacts by surface heat and freshwater perturbations. In terms of impacts on the subpolar SO and AABW, Dias et al. (2021) found that the expected wind forcing due to doubling of CO_2 completely overshadows any effects from surface heat and freshwater fluxes. However, Dias et al. (2021) did not consider any additional freshening due to AIS melting. In contrast, we have shown for both CM4 and ESM4 that it is the freshening around Antarctica due to the addition of AIS meltwater that defines the transient response of the SO MOC in the combined forcing scheme (AntwaterStress), which underscores the importance of accurately simulating the melting of ice sheets around Antarctica. In the traditional experiments within FAFMIP, atmospheric freshwater flux changes from $2xCO_2$ are not enough to counteract wind stress perturbations. An important consequence of our findings and those of Beadling et al. (2022) are that the SO response is dominated by meltwater. Since these perturbations are derived from a $2xCO_2$ simulation, this result supports the idea that the inclusion of AIS meltwater fluxes are necessary to derive more robust future projections of water mass changes in this region and thus global climate projections (Bronselaer et al., 2018).

4.2 Surface WMT over the Antarctic shelf as a key factor in model response

Given that the signature changes in SO MOC, and especially concerning AABW, are almost entirely due to the Antarctic meltwater additions, the transient state in the combined forcing experiment is defined by a slowing bottom overturning and declining AABW volume. When considering the overturning at 30°S and comparing it to the changes in WMT and volume south of 30°S, we saw that CM4 and ESM4 respond very differently to increased AIS melting. How surface-forced transformation is affected in the high-end density range ($\sigma_2 > 37.2$) was identified as the key factor in determining the transient response in the deep SO. Importantly, isopycnals corresponding to this density are mostly outcropping over the Antarctic shelf. Thus, DSW formation from brine rejection and the extent to how much the additional meltwater from the AIS is impacting this process are crucial for an accurate representation of AABW in climate models. In CM4, the meltwater perturbation eliminates surface-forced densification corresponding to DSW ($\sigma_2 > 37.2$), leading to immediate deflation of AABW and a gradual weakening of the

lower limb overturning. In contrast, surface formation of DSW is still present in ESM4 even at 50 years after the additional Antarctic melting was imposed. Hence, the meltwater experiment in ESM4 still has AABW formation due to shelf convection. We thus find that the impact of Antarctic melt perturbations to the deep SO is fundamentally different in ESM4 compared to CM4.

Beadling et al. (2022) documented important differences in the representation of the ASC between CM4 and ESM4. In particular, in the model's mean state, the ASC is stronger and more well-defined along the continental slope in CM4, whereas in ESM4 the ASC is represented by a much weaker and broader off-shelf flow, roughly half in magnitude compared to CM4. Furthermore, added meltwater on the Antarctic shelf leads to a strong circumpolar acceleration of the ASC in CM4, which is also seen in ESM4, but of much lesser magnitude (Beadling et al., 2022). When Antarctic meltwater is imposed, deep homogenous fresh anomalies start to develop over the Antarctic shelf in CM4. This freshening over the Antarctic shelf is much more pronounced in CM4 compared to ESM4. Freshening of the shelf enhances the lateral density gradient between the shelf and the open ocean, which in turn causes the ASC to accelerate. This response leads to a positive feedback in which the stronger ASC leads to reduced cross-slope exchanges such that meltwater effectively becomes trapped on the shelf, leading to further shelf freshening and further acceleration of the ASC. On the other hand, the less refined ASC in ESM4 does not accelerate as much, and a large fraction of the AIS meltwater is transported off the shelf. Thus, the fresh anomalies on the shelf are less pronounced in ESM4 compared to CM4, and there is no reinforcing feedback between shelf freshening and ASC strengthening.

Beadling et al. (2022) showed that this differing response along the Antarctic shelf has important consequences on heat transfer towards the Antarctic margins and suggested that projections of ocean-driven melting of the AIS may depend on how well a model resolves the ASC. The results of the Antwater simulation with the 0.25° CM4 model confirms previous high-resolution modeling studies, where Antarctic melting leads to a negative feedback in which the Antarctic shelf becomes isolated from the upwelling of warm CDW, potentially inhibiting further basal melting (Goddard et al., 2017; Moorman et al., 2020). On the other hand, results from the 0.5° ESM4 model reflects findings by relatively coarse resolution models showing a positive feedback where Antarctic melting enhances shoreward heat transport, leading to more subsurface warming around Antarctica and potentially further increasing Antarctic mass loss (Bronselaer et al., 2018; Golledge et al., 2019). As noted previously, there are several important component differences between CM4 and ESM4 beyond their respective resolutions and representation of the ASC. For example, the higher snow-on-glacier albedo in ESM4 could also play a role in the reduced sensitivity of AABW to these perturbations. Here we add to the results of Beadling et al. (2022) and show that the different representation of the ASC in the two models is likely the key factor in how AABW is projected to change in response to enhanced melting of the AIS.

Since the AIS meltwater is being held on the shelf by a stronger ASC in the CM4 Antwater experiment, it is readily redistributed by the shelf current system, leading to a homogeneous freshening across the entire shelf, including DSW formation regions (Weddell shelf, Prydz Bay, Adelie Coast and Ross shelf). The surface and subsurface freshening leads to an overall reduction in density. This response can be seen in a shift of the maximum surface WMT over the continental shelf towards lighter densities in Figure 10. Shelf waters are still being made denser by brine rejection associated with sea ice growth over the DSW formation regions. However, surface-forced formation is below the density required for DSW ($\sigma_2 > 37.2$) to support overflows and bottom water formation. The Antarctic melt perturbation in ESM4 does not result in a strong homogenized shelf freshening as observed in CM4. Given the same AIS meltwater input, more freshwater enters the open ocean in ESM4 due to the weaker ASC relative to CM4, allowing for more

cross-shelf exchange. Water mass formation by brine rejection in ESM4 is reduced by ∼50%, but still present in the DSW density class, allowing for dense enough waters in ESM4 to descend at depth and contribute to AABW.

As implied by positive volume changes in the deep Weddell Sea (Figure 8), bottom water is still being formed on the Weddell shelf throughout the Antwater experiment in ESM4. This formation is consistent with the spatial distribution of the meltwater sources around Antarctica. The largest observed mass loss from the AIS is occurring in West Antarctica (Paolo et al., 2015; Smith et al., 2020). The imposed Antarctic meltwater fluxes are redistributed westward towards the Ross shelf with less direct meltwater input in the Weddell region. Thus, DSW is still being produced at high enough densities in the Weddell shelf to sink to the deep Weddell Sea and contribute to AABW (Figure 11c). This situation points to the potential importance in accurately defining the location of meltwater input around the shelf. Previous work suggested little sensitivity to the spatial distribution of Antarctic melting based on uniform patterns of prescribed melting (Lago & England, 2019). In our experimental design, the additional melting was based on observed ice shelf melting. In the case of ESM4, this spatial non-uniformity allowed the Weddell shelf to be less impacted by the meltwater forcing than if the same amount of meltwater (0.1 Sv) was prescribed as in previous designs (e.g., Bronselaer et al., 2018; Lago & England, 2019).

The striking mismatch between CM4 and ESM4 in Antarctic shelf and AABW response under the same meltwater perturbation underscores the relevance of representing DSW formation processes in climate models. This emphasis is in contrast to the considerable fraction of AABW formation from open-ocean convection observed in many climate models. Even though dense water formation occurs via open-ocean polynya events during the Control simulation in CM4 and ESM4, these intermittent bottom water formation events are absent in the Antwater simulations for both models (Beadling et al., 2022). However, the strong volume loss in AABW is only seen in CM4, even though the shutoff of deep convection events within the open ocean occurs in both models. Thus, it is the change in dense water formation over the Antarctic shelf that is the key in understanding the mismatch in AABW volume response between the two models. This conclusion is consistent with findings presented in Lago and England (2019) who showed that it is the decline in shelf convection that is driving the collapse of AABW in their meltwater experiments, despite the open-ocean estimate comprising almost half of the total convection in the control state.

4.3 Role of overturning versus ventilation in defining the SO's transient response

In response to Antarctic melting increases, the contraction of the AABW volume south of 30°S is much stronger in CM4 compared to ESM4. On the other hand, the decline in the overturning at 30°S is approximately the same in the two models. This behavior highlights the potential for a disconnect between processes associated with the ventilation of the deep SO and those maintaining meridional volume transports between the SO and the deep basins of the Atlantic, Indian and Pacific Ocean. This important distinction between overturning and ventilation has been documented for the mode and intermediate waters of the SO (Morrison et al., 2022). Here we used the WMT framework to disentangle the impacts on ventilation and overturning regarding the transient response in the deep SO.

Overturning has been used as a metric of constituent transport into the deep ocean. However, it has been shown that transport processes relevant to heat and carbon are often disconnected from overturning. For example, MacGilchrist et al. (2019) identified that it was not the overturning that was controlling the transport of carbon, but actually the horizontal circulation and water masses within the Weddell gyre. Our analysis

used a comprehensive assessment of the response in deep SO water masses to given changes in surface forcing, which considered overturning as a balance between storage change and WMT. From this framework, it becomes apparent that a change in surface forcing (i.e., changes in water formation/destruction at the surface) does not directly impact overturning, but instead translates to changes in interior mixing processes, which in turn impact the volume of a given water mass before meridional transports are affected.

Consequently, the fidelity with which a model can resolve the mixing terms is highly important. The substantial role of interior WMT in establishing the SO MOC has been previously documented (Iudicone et al., 2008; Downes et al., 2011; Cerovečki et al., 2013; Newsom et al., 2016). An important point to make is that changes in surface forcing are directly compensated by mixing in the short term. This compensation represents impacts on ventilation that are relevant for the uptake of ocean constituents. On the other hand, the long-term balance between surface and interior WMT with storage change becomes relevant in understanding the transient adjustment of SO MOC. In particular, for understanding the response in the lower limb overturning, it is important to consider a balance between WMT and volume changes along with the overturning streamfunction.

In this study, the contribution by interior WMT needs to be inferred from Equation (6), since appropriate model diagnostics were not available. Future work is encouraged to better characterize the diapycnal mixing processes associated with interior WMT. Previous work has provided insights on where the majority of interior WMT occurs (e.g., Iudicone et al., 2008; Urakawa et al., 2020). For most of the SO, entrainment and detrainment at the base of the mixed layer, as well as eddy-driven mixing within the mixed layer, are both important processes (Iudicone et al., 2008), with diapycnal mixing in the deep interior ocean (below the mixed layer) playing only a secondary role. Resolving the subsurface mixing component is challenging because it contains both explicit mixing processes as well as spurious or numerical mixing (S. M. Griffies et al., 2000; Lee et al., 2002). In terms of future modeling work, interior WMT can be resolved from heat and salt tendencies due to vertical and lateral mixing (e.g., Iudicone et al., 2008), with lateral mixing processes related to the nonlinear equation of state, such as cabbeling and thermobaricity (Nycander et al., 2015; Groeskamp et al., 2016).

5 Conclusion

In this study we used two similar coupled models (GFDL CM4 and ESM4) that mainly differ in their horizontal resolution and representation of mesoscale eddies to investigate the response of Southern Ocean (SO) overturning, water mass transformations, and ventilation to projected changes in wind forcing and Antarctic Ice sheet (AIS) meltwater. Similar to previous work, we see that stronger and poleward shifted westerlies enhance bottom overturning, while adding AIS meltwater weakens it. We found that when imposing the two forcings simultaneously, AIS meltwater dominates the response in the SO meridional overturning circulation (SO MOC), with changes in meridional transport at 30°S being very similar between the two models. However, the transient response to meltwater is very different between the models south of 30°S, when considering the balance between overturning, water mass transformation and layer volume changes in the deep SO. We found that surface and interior transformation processes south of 30°S respond differently between the models resulting in starkly different AABW changes in the two models.

Beadling et al. (2022) established that the mean-state strength, structure, and meltwater-driven acceleration of the Antarctic Slope Current (ASC) was the key to explaining the striking difference in the thermal response along the Antarctic shelf between the two models. We expand on Beadling et al. (2022) and show that the ASC also plays a central role in explaining the starkly different evolutions of AABW in response to the meltwater forcing through its influence on dense shelf water (DSW) formation and subsequent over-

flow to the deep ocean. The freshwater trapped by the stronger and accelerating ASC in CM4 leads to a shut down of DSW in CM4, while DSW formation and overflow to the deep ocean continues in ESM4. This contrasting response leads to characteristically different responses in interior mixing. A larger interior destruction of AABW volume occurs in CM4, coinciding with a stronger deflation of AABW relative to ESM4.

Given the role of AABW as a pathway to sequester heat and carbon into the deep ocean on long time scales (Marinov et al., 2006; DeVries et al., 2012), the strikingly different response of AABW volume between the two models has important ramifications for how these two models may project the oceanic uptake of heat and carbon in future climate scenarios. This study suggests that under ongoing climate change, models with sufficient horizontal resolutions for a coherent ASC around the Antarctic continental margin may simulate a stronger decline in future heat and carbon uptake by reducing the formation and export of DSW to the deep SO. On the other hand, models with an unresolved or less defined ASC are more likely to continue sequestering heat and carbon into the deep ocean through DSW and subsequent AABW formation processes. We argue that, through its direct impact on the projected evolution of the densification of surface waters and export of AABW to the deep ocean, whether a coherent ASC is present in a model or not has important consequences on its ability to accurately project atmospheric CO_2 concentration, (DeVries et al., 2017; Kessler & Tjiputra, 2016; Watson et al., 2020; Nissen et al., 2022), regional and global mean temperature (Pierce et al., 2012; Sallée, 2018; Hobbs et al., 2021; Lin et al., 2021), and sea level changes (Church et al., 2013; Couldrey et al., 2021). The diverging responses of the deep SO to surface wind stress and meltwater perturbations due to differences in ASC, which are mainly dependent on the horizontal resolution of a model (Dufour et al., 2017; Goddard et al., 2017; Lockwood et al., 2021), point to an important source of uncertainty when considering the future evolution of the SO and global climate.

Open Research

Model data from the preindustrial control (piControl) runs of CM4 and ESM4 are available at the Earth System Grid Federation archive (`https://esgf-node.llnl.gov/projects/cmip6`). Model output from the wind and Antarctic meltwater experiments will be made publicly available on the same archive as part of the FAFMIP contribution to CMIP6 and can be retrieved at (Zenodo link will be inserted here at time of acceptance). The forcing fields used in these experiments can be found at `https://github.com/becki-beadling/Beadling_et_al_2022_JGROceans`. The GFDL MOM6 code is available at `https://github.com/NOAA-GFDL/MOM6`. Water mass transformation calculations were done using the python package xwmt (`https://github.com/jetesdal/xwmt`). Python scripts and Jupyter notebooks along with interim datasets to reproduce the tables and figures can be accessed at (GitHub link will be inserted here at time of acceptance).

Acknowledgments

This work was performed under the auspices of the U.S. Department of Energy by Lawrence Livermore National Laboratory (LLNL) under Contract DE-AC52-07NA27344. It is a contribution to the science portfolio of the U.S. Department of Energy, Office of Science, Earth and Environmental Systems Sciences Division, Regional and Global Model Analysis Program. JET and GAM acknowledge funding from LLNL under Subcontract no. B640108. RLB was funded by the NOAA Climate and Global Change postdoctoral program. GAM was additionally supported by funds from NSF (PLR-1425989) and NASA (80NSSC19K1115). The work of PJD is supported by the U.S. Department of Energy, Office of Science, Earth and Environmental Systems Sciences Division, Regional and Global Model Analysis Program. LLNL Release Number: LLNL-JNRL-836389. Data analysis relied on the Python programming language (`https://www.python.org`), in particular

the packages xarray (`http://xarray.pydata.org`), pandas (`https://pandas.pydata.org`), and xgcm (`https://xgcm.readthedocs.io`). The authors wish to thank the FAFMIP team for production of the wind stress perturbation fields. We are grateful for very helpful comments and suggestions by John Dunne, Liping Zhang and Raphael Dussin at NOAA's Geophysical Fluid Dynamics Laboratory. The computational resources that allowed for the analysis presented in this manuscript sit on the ancient homeland and traditional territory of the Lenape people. The authors pay respect to Lenape peoples past, present, and future and their continuing presence in the homeland and throughout the Lenape diaspora.

Appendix A List of Acronyms

AABW	Antarctic Bottom Water
AAIW	Antarctic Intermediate Water
AIS	Antarctic Ice Sheet
ASC	Antarctic Slope Current
CDW	Circumpolar Deep Water
DSW	Dense Shelf Water
GFDL	Geophysical Fluid Dynamics Laboratory
MLD	Mixed Layer Depth
MOC	Meridional Overturning Circulation
NADW	North Atlantic Deep Water
NOAA	National Oceanic and Atmospheric Administration
SAMW	Subantarctic Mode Water
SO	Southern Ocean
WMT	Water Mass Transformation

References

Abernathey, R. P., Cerovecki, I., Holland, P. R., Newsom, E., Mazloff, M., & Talley, L. D. (2016). Water-mass transformation by sea ice in the upper branch of the southern ocean overturning. *Nature Geoscience*, *9*, 596-601. doi: 10.1038/ngeo2749

Adcroft, A., Anderson, W., Balaji, V., Blanton, C., Bushuk, M., Dufour, C. O., ... Zhang, R. (2019). The gfdl global ocean and sea ice model om4.0: Model description and simulation features. *Journal of Advances in Modeling Earth Systems*, *11*(10), 3167-3211. doi: 10.1029/2019MS001726

Aguiar, W., Mata, M. M., & Kerr, R. (2017). On deep convection events and Antarctic Bottom Water formation in ocean reanalysis products. *Ocean Science*, *13*(6), 851–872. doi: 10.5194/os-13-851-2017

Akhoudas, C. H., Sallée, J.-B., Haumann, F. A., Meredith, M. P., Garabato, A. N., Reverdin, G., ... Arrowsmith, C. (2021). Ventilation of the abyss in the Atlantic sector of the Southern Ocean. *Scientific Reports*, *11*(1), 6760. doi: 10.1038/s41598-021-86043-2

Anilkumar, N., Chacko, R., Sabu, P., & George, J. V. (2015). Freshening of Antarctic Bottom Water in the Indian Ocean sector of Southern Ocean. *Deep Sea Research Part II: Topical Studies in Oceanography*, *118*, 162–169. doi: 10.1016/j.dsr2.2015.03.009

Anilkumar, N., Jena, B., George, J. V., P, S., S, K., & Ravichandran, M. (2021). Recent Freshening, Warming, and Contraction of the Antarctic Bottom Water in the Indian Sector of the Southern Ocean. *Frontiers in Marine Science*, *8*, 730630. doi: 10.3389/fmars.2021.730630

Azaneu, M., Kerr, R., Mata, M. M., & Garcia, C. A. E. (2013). Trends in the deep Southern Ocean (1958–2010): Implications for Antarctic Bottom Water properties and volume export. *Journal of Geophysical Research: Oceans*, *118*(9),

4213–4227. doi: 10.1002/jgrc.20303

Beadling, R. L., Krasting, J. P., Griffies, S., Hurlin, W. J., Bronselear, B., Russell, J. L., ... Winton, M. (2022). Importance of the Antarctic Slope Current in the Southern Ocean Response to Ice Sheet Melt and Wind Stress Change. *Journal of Geophysical Research: Oceans*.

Bernardello, R., Marinov, I., Palter, J. B., Galbraith, E. D., & Sarmiento, J. L. (2014). Impact of Weddell Sea deep convection on natural and anthropogenic carbon in a climate model. *Geophysical Research Letters*, *41*(20), 7262–7269. doi: 10.1002/2014gl061313

Bintanja, R., Oldenborgh, G. J. v., Drijfhout, S. S., Wouters, B., & Katsman, C. A. (2013). Important role for ocean warming and increased ice-shelf melt in Antarctic sea-ice expansion. *Nature Geoscience*, *6*(5), 376–379. doi: 10.1038/ngeo1767

Bishop, S. P., Gent, P. R., Bryan, F. O., Thompson, A. F., Long, M. C., & Abernathey, R. (2016). Southern Ocean Overturning Compensation in an Eddy-Resolving Climate Simulation. *Journal of Physical Oceanography*, *46*(5), 1575–1592. doi: 10.1175/jpo-d-15-0177.1

Bronselaer, B., Russell, J. L., Winton, M., Williams, N. L., Key, R. M., Dunne, J. P., ... Sarmiento, J. L. (2020). Importance of wind and meltwater for observed chemical and physical changes in the Southern Ocean. *Nature Geoscience*, *13*(1), 35–42. doi: 10.1038/s41561-019-0502-8

Bronselaer, B., Winton, M., Griffies, S. M., Hurlin, W. J., Rodgers, K. B., Sergienko, O. V., ... Russell, J. L. (2018). Change in future climate due to Antarctic meltwater. *Nature*, *564*(7734), 53–58. doi: 10.1038/s41586-018-0712-z

Bryan, F. O., Danabasoglu, G., Nakashiki, N., Yoshida, Y., Kim, D.-H., Tsutsui, J., & Doney, S. C. (2006). Response of the North Atlantic Thermohaline Circulation and Ventilation to Increasing Carbon Dioxide in CCSM3. *Journal of Climate*, *19*(11), 2382–2397. doi: 10.1175/jcli3757.1

Caldeira, K., & Duffy, P. B. (2000). The Role of the Southern Ocean in Uptake and Storage of Anthropogenic Carbon Dioxide. *Science*, *287*(5453), 620–622. doi: 10.1126/science.287.5453.620

Cerovečki, I., Talley, L. D., Mazloff, M. R., & Maze, G. (2013). Subantarctic Mode Water Formation, Destruction, and Export in the Eddy-Permitting Southern Ocean State Estimate. *Journal of Physical Oceanography*, *43*(7), 1485–1511. doi: 10.1175/JPO-D-12-0121.1

Cessi, P. (2019). The Global Overturning Circulation. *Annual Review of Marine Science*, *11*(1), 249–270. doi: 10.1146/annurev-marine-010318-095241

Chen, X., & Tung, K.-K. (2014). Varying planetary heat sink led to global-warming slowdown and acceleration. *Science*, *345*(6199), 897–903. doi: 10.1126/science.1254937

Church, J. A., Monselesan, D., Gregory, J. M., & Marzeion, B. (2013). Evaluating the ability of process based models to project sea-level change. *Environmental Research Letters*, *8*(1), 014051. doi: 10.1088/1748-9326/8/1/014051

Couldrey, M. P., Gregory, J. M., Dias, F. B., Dobrohotoff, P., Domingues, C. M., Garuba, O., ... Zanna, L. (2021). What causes the spread of model projections of ocean dynamic sea-level change in response to greenhouse gas forcing? *Climate Dynamics*, *56*(1-2), 155–187. doi: 10.1007/s00382-020-05471-4

Davies, J. H. (2013). Global map of solid Earth surface heat flow. *Geochemistry, Geophysics, Geosystems*, *14*(10), 4608–4622. doi: 10.1002/ggge.20271

DeConto, R. M., & Pollard, D. (2016). Contribution of Antarctica to past and future sea-level rise. *Nature*, *531*(7596), 591–597. doi: 10.1038/nature17145

de Lavergne, C., Madec, G., Sommer, J. L., Nurser, A. J. G., & Garabato, A. C. N. (2016). On the Consumption of Antarctic Bottom Water in the Abyssal Ocean. *Journal of Physical Oceanography*, *46*(2), 635–661. doi: 10.1175/jpo-d-14-0201.1

de Lavergne, C. d., Palter, J. B., Galbraith, E. D., Bernardello, R., & Marinov, I. (2014). Cessation of deep convection in the open Southern Ocean under anthropogenic climate change. *Nature Climate Change*, *4*(4), 278–282. doi: 10.1038/nclimate2132

Delworth, T. L., Cooke, W. F., Adcroft, A., Bushuk, M., Chen, J., Dunne, K. A., ... Zhao, M. (2020). SPEAR: The Next Generation GFDL Modeling System for Seasonal to Multidecadal Prediction and Projection. *Journal of Advances in Modeling Earth Systems*, *12*(3). doi: 10.1029/2019ms001895

DeVries, T., Holzer, M., & Primeau, F. (2017). Recent increase in oceanic carbon uptake driven by weaker upper-ocean overturning. *Nature*, *542*(7640), 215–218. doi: 10.1038/nature21068

DeVries, T., Primeau, F., & Deutsch, C. (2012). The sequestration efficiency of the biological pump. *Geophysical Research Letters*, *39*(13). doi: 10.1029/2012gl051963

Dias, F. B., Domingues, C. M., Marsland, S. J., Rintoul, S. R., Uotila, P., Fiedler, R., ... Savita, A. (2021). Subpolar Southern Ocean Response to Changes in the Surface Momentum, Heat, and Freshwater Fluxes under 2xCO_2. *Journal of Climate*, *34*(21), 8755–8775. doi: 10.1175/jcli-d-21-0161.1

Döös, K., & Webb, D. J. (1994). The Deacon Cell and the Other Meridional Cells of the Southern Ocean. *Journal of Physical Oceanography*, *24*(2), 429–442. doi: 10.1175/1520-0485(1994)024⟨0429:tdcato⟩2.0.co;2

Downes, S. M., Gnanadesikan, A., Griffies, S. M., & Sarmiento, J. L. (2011). Water Mass Exchange in the Southern Ocean in Coupled Climate Models. *Journal of Physical Oceanography*, *41*(9), 1756–1771. doi: 10.1175/2011JPO4586.1

Downes, S. M., Langlais, C., Brook, J. P., & Spence, P. (2017). Regional Impacts of the Westerly Winds on Southern Ocean Mode and Intermediate Water Subduction. *Journal of Physical Oceanography*, *47*(10), 2521–2530. doi: 10.1175/JPO-D-17-0106.1

Dufour, C. O., Morrison, A. K., Griffies, S. M., Frenger, I., Zanowski, H., & Winton, M. (2017). Preconditioning of the Weddell Sea Polynya by the Ocean Mesoscale and Dense Water Overflows. *Journal of Climate*, *30*(19), 7719–7737. doi: 10.1175/jcli-d-16-0586.1

Dunne, J. P., Horowitz, L. W., Adcroft, A. J., Ginoux, P., Held, I. M., John, J. G., ... Zhao, M. (2020). The GFDL Earth System Model Version 4.1 (GFDL-ESM 4.1): Overall Coupled Model Description and Simulation Characteristics. *Journal of Advances in Modeling Earth Systems*, *12*(11). doi: 10.1029/2019ms002015

Eyring, V., Bony, S., Meehl, G. A., Senior, C. A., Stevens, B., Stouffer, R. J., & Taylor, K. E. (2016). Overview of the Coupled Model Intercomparison Project Phase 6 (CMIP6) experimental design and organization. *Geoscientific Model Development*, *9*(5), 1937–1958. doi: 10.5194/gmd-9-1937-2016

Farneti, R., & Delworth, T. L. (2010). The Role of Mesoscale Eddies in the Remote Oceanic Response to Altered Southern Hemisphere Winds. *Journal of Physical Oceanography*, *40*(10), 2348–2354. doi: 10.1175/2010jpo4480.1

Farneti, R., Delworth, T. L., Rosati, A. J., Griffies, S. M., & Zeng, F. (2010). The Role of Mesoscale Eddies in the Rectification of the Southern Ocean Response to Climate Change. *Journal of Physical Oceanography*, *40*(7), 1539–1557. doi: 10.1175/2010jpo4353.1

Farneti, R., Downes, S. M., Griffies, S. M., Marsland, S. J., Behrens, E., Bentsen, M., ... Yeager, S. G. (2015). An assessment of Antarctic Circumpolar Current and Southern Ocean meridional overturning circulation during 1958–2007 in a suite of interannual CORE-II simulations. *Ocean Modelling*, *93*, 84–120. doi: 10.1016/j.ocemod.2015.07.009

Farneti, R., & Gent, P. R. (2011). The effects of the eddy-induced advection coefficient in a coarse-resolution coupled climate model. *Ocean Modelling*, *39*(1-2),

135–145. doi: 10.1016/j.ocemod.2011.02.005

Fogt, R. L., & Marshall, G. J. (2020). The Southern Annular Mode: Variability, trends, and climate impacts across the Southern Hemisphere. *Wiley Interdisciplinary Reviews: Climate Change*, *11*(4). doi: 10.1002/wcc.652

Fogwill, C. J., Phipps, S. J., Turney, C. S. M., & Golledge, N. R. (2015). Sensitivity of the Southern Ocean to enhanced regional Antarctic ice sheet meltwater input. *Earth's Future*, *3*(10), 317–329. doi: 10.1002/2015ef000306

Frölicher, T. L., Sarmiento, J. L., Paynter, D. J., Dunne, J. P., Krasting, J. P., & Winton, M. (2015). Dominance of the Southern Ocean in Anthropogenic Carbon and Heat Uptake in CMIP5 Models. *Journal of Climate*, *28*(2), 862–886. doi: 10.1175/jcli-d-14-00117.1

Gao, L., Rintoul, S. R., & Yu, W. (2018). Recent wind-driven change in Subantarctic Mode Water and its impact on ocean heat storage. *Nature Climate Change*, *8*(1), 58–63. doi: 10.1038/s41558-017-0022-8

Gent, P. R., & Danabasoglu, G. (2011). Response to Increasing Southern Hemisphere Winds in CCSM4. *Journal of Climate*, *24*(19), 4992–4998. doi: 10.1175/jcli-d-10-05011.1

Gent, P. R., Willebrand, J., McDougall, T. J., & McWilliams, J. C. (1995). Parameterizing eddy-induced tracer transports in ocean circulation models. *Journal of Physical Oceanography*, *25*, 463–474. doi: 10.1175/1520-0485(1995)025⟨0463:PEITTI⟩2.0.CO;2

Gnanadesikan, A. (1999). A Simple Predictive Model for the Structure of the Oceanic Pycnocline. *Science*, *283*(5410), 2077–2079. doi: 10.1126/science.283.5410.2077

Goddard, P., Dufour, C., Yin, J., Griffies, S. M., & Winton, M. (2017). CO_2-induced ocean warming of the Antarctic continental shelf in an eddying global climate model. *Journal of Geophysical Research - Oceans*, *122*. doi: 10.1002/2017JC012849

Golledge, N. R., Keller, E. D., Gomez, N., Naughten, K. A., Bernales, J., Trusel, L. D., & Edwards, T. L. (2019). Global environmental consequences of twenty-first-century ice-sheet melt. *Nature*, *566*(7742), 65–72. doi: 10.1038/s41586-019-0889-9

Goyal, R., Gupta, A. S., Jucker, M., & England, M. H. (2021). Historical and Projected Changes in the Southern Hemisphere Surface Westerlies. *Geophysical Research Letters*, *48*(4). doi: 10.1029/2020gl090849

Gregory, J. M., Bouttes, N., Griffies, S. M., Haak, H., Hurlin, W. J., Jungclaus, J., ... Winton, M. (2016). The Flux-Anomaly-Forced Model Intercomparison Project (FAFMIP) contribution to CMIP6: investigation of sea-level and ocean climate change in response to CO_2 forcing. *Geoscientific Model Development*, *9*(11), 3993–4017. doi: 10.5194/gmd-9-3993-2016

Griffies, S., Adcroft, A., & Hallberg, R. (2020). A primer on the vertical lagrangian-remap method in ocean models based on finite volume generalized vertical coordinates. *Journal of Advances in Modeling Earth Systems*, *12*. doi: 10.1029/2019MS001954

Griffies, S. M., Pacanowski, R. C., & Hallberg, R. W. (2000). Spurious diapycnal mixing associated with advection in a z-coordinate ocean model. *Monthly Weather Review*, *128*, 538–564. doi: 10.1175/1520-0493(2000)128⟨0538:SDMAWA⟩2.0.CO;2

Grist, J. P., Josey, S. A., & Marsh, R. (2012). Surface estimates of the Atlantic overturning in density space in an eddy-permitting ocean model. *Journal of Geophysical Research: Oceans (1978–2012)*, *117*(C6). doi: 10.1029/2011jc007752

Grist, J. P., Josey, S. A., Marsh, R., Kwon, Y.-O., Bingham, R. J., & Blaker, A. T. (2014). The Surface-Forced Overturning of the North Atlantic: Estimates from Modern Era Atmospheric Reanalysis Datasets. *Journal of Climate*, *27*(10), 3596–3618. doi: 10.1175/jcli-d-13-00070.1

Grist, J. P., Marsh, R., & Josey, S. A. (2009). On the Relationship between the North Atlantic Meridional Overturning Circulation and the Surface-Forced Overturning Streamfunction. *Journal of Climate*, *22*(19), 4989–5002. doi: 10.1175/2009jcli2574.1

Groeskamp, S., Abernathey, R. P., & Klocker, A. (2016). Water mass transformation by cabbeling and thermobaricity. *Geophysical Research Letters*, *43*(20), 10835–10845. doi: 10.1002/2016gl070860

Groeskamp, S., Griffies, S. M., Iudicone, D., Marsh, R., Nurser, A. J. G., & Zika, J. D. (2019). The Water Mass Transformation Framework for Ocean Physics and Biogeochemistry. *Annual Review of Marine Science*, *11*(1), 271–305. doi: 10.1146/annurev-marine-010318-095421

Groeskamp, S., & Iudicone, D. (2018). The Effect of Air-Sea Flux Products, Shortwave Radiation Depth Penetration, and Albedo on the Upper Ocean Overturning Circulation. *Geophysical Research Letters*, *45*(17), 9087–9097. doi: 10.1029/2018gl078442

Gupta, A. S., Jourdain, N. C., Brown, J. N., & Monselesan, D. (2013). Climate Drift in the CMIP5 Models. *Journal of Climate*, *26*(21), 8597–8615. doi: 10.1175/jcli-d-12-00521.1

Haumann, F. A., Gruber, N., Münnich, M., Frenger, I., & Kern, S. (2016). Sea-ice transport driving Southern Ocean salinity and its recent trends. *Nature*, *537*(7618), 89–92. doi: 10.1038/nature19101

Held, I. M., Guo, H., Adcroft, A., Dunne, J. P., Horowitz, L. W., Krasting, J., ... Zadeh, N. (2019). Structure and Performance of GFDL's CM4.0 Climate Model. *Journal of Advances in Modeling Earth Systems*, *11*(11), 3691–3727. doi: 10.1029/2019ms001829

Heuzé, C. (2021). Antarctic Bottom Water and North Atlantic Deep Water in CMIP6 models. *Ocean Science*, *17*(1), 59–90. doi: 10.5194/os-17-59-2021

Heuzé, C., Heywood, K. J., Stevens, D. P., & Ridley, J. K. (2015). Changes in Global Ocean Bottom Properties and Volume Transports in CMIP5 Models under Climate Change Scenarios. *Journal of Climate*, *28*(8), 2917–2944. doi: 10.1175/jcli-d-14-00381.1

Hirst, A. C., & McDougall, T. J. (1998). Meridional Overturning and Dianeutral Transport in a z-Coordinate Ocean Model Including Eddy-Induced Advection. *Journal of Physical Oceanography*, *28*(6), 1205–1223. doi: 10.1175/1520-0485(1998)028⟨1205:moadti⟩2.0.co;2

Hobbs, W. R., Roach, C., Roy, T., Sallée, J.-B., & Bindoff, N. (2021). Anthropogenic Temperature and Salinity Changes in the Southern Ocean. *Journal of Climate*, *34*(1), 215–228. doi: 10.1175/jcli-d-20-0454.1

Hogg, A. M., Spence, P., Saenko, O. A., & Downes, S. M. (2017). The Energetics of Southern Ocean Upwelling. *Journal of Physical Oceanography*, *47*(1), 135–153. doi: 10.1175/jpo-d-16-0176.1

Irving, D., Hobbs, W., Church, J., & Zika, J. (2021). A Mass and Energy Conservation Analysis of Drift in the CMIP6 Ensemble. *Journal of Climate*, *34*(8), 3157–3170. doi: 10.1175/jcli-d-20-0281.1

Iudicone, D., Madec, G., Blanke, B., & Speich, S. (2008). The Role of Southern Ocean Surface Forcings and Mixing in the Global Conveyor. *Journal of Physical Oceanography*, *38*(7), 1377–1400. doi: 10.1175/2008jpo3519.1

Jansen, M., & Held, I. (2014). Parameterizing subgrid-scale eddy effects using energetically consistent backscatter. *Ocean Modelling*, *80*, 36–48. doi: 10.1016/j.ocemod.2014.06.002

Kessler, A., & Tjiputra, J. (2016). The Southern Ocean as a constraint to reduce uncertainty in future ocean carbon sinks. *Earth System Dynamics*, *7*(2), 295–312. doi: 10.5194/esd-7-295-2016

Lago, V., & England, M. H. (2019). Projected slowdown of Antarctic Bottom Water formation in response to amplified meltwater contributions. *Journal of Cli-*

mate, *32*(19), 6319–6335. doi: 10.1175/jcli-d-18-0622.1

Lee, M.-M., & Coward, A. (2003). Eddy mass transport for the Southern Ocean in an eddy-permitting global ocean model. *Ocean Modelling*, *5*(3), 249–266. doi: 10.1016/s1463-5003(02)00044-6

Lee, M.-M., Coward, A. C., & Nurser, A. J. G. (2002). Spurious Diapycnal Mixing of the Deep Waters in an Eddy-Permitting Global Ocean Model. *Journal of Physical Oceanography*, *32*(5), 1522–1535. doi: 10.1175/1520-0485(2002)032⟨1522:sdmotd⟩2.0.co;2

Legg, S., Hallberg, R. W., & Girton, J. B. (2006). Comparison of entrainment in overflows simulated by z-coordinate, isopycnal and non-hydrostatic models. *Ocean Modelling*, *11*(1-2), 69–97. doi: 10.1016/j.ocemod.2004.11.006

Lin, Y., Hwang, Y., Lu, J., Liu, F., & Rose, B. E. J. (2021). The Dominant Contribution of Southern Ocean Heat Uptake to Time-Evolving Radiative Feedback in CESM. *Geophysical Research Letters*, *48*(9). doi: 10.1029/2021gl093302

Lockwood, J. W., Dufour, C. O., Griffies, S. M., & Winton, M. (2021). On the Role of the Antarctic Slope Front on the Occurrence of the Weddell Sea Polynya under Climate Change. *Journal of Climate*, *34*(7), 2529–2548. doi: 10.1175/jcli-d-20-0069.1

Lumpkin, R., & Speer, K. (2007). Global Ocean Meridional Overturning. *Journal of Physical Oceanography*, *37*(10), 2550–2562. doi: 10.1175/JPO3130.1

MacGilchrist, G. A., Garabato, A. C. N., Brown, P. J., Jullion, L., Bacon, S., Bakker, D. C. E., ... Torres-Valdés, S. (2019). Reframing the carbon cycle of the subpolar Southern Ocean. *Science Advances*, *5*(8), eaav6410. doi: 10.1126/sciadv.aav6410

Mackie, S., Smith, I. J., Ridley, J. K., Stevens, D. P., & Langhorne, P. J. (2020). Climate Response to Increasing Antarctic Iceberg and Ice Shelf Melt. *Journal of Climate*, *33*(20), 8917–8938. doi: 10.1175/jcli-d-19-0881.1

Marinov, I., Gnanadesikan, A., Toggweiler, J. R., & Sarmiento, J. L. (2006). The Southern Ocean biogeochemical divide. *Nature*, *441*(7096), 964–967. doi: 10.1038/nature04883

Marsh, R. (2000). Recent Variability of the North Atlantic Thermohaline Circulation Inferred from Surface Heat and Freshwater Fluxes. *Journal of Climate*, *13*(18), 3239–3260. doi: 10.1175/1520-0442(2000)013⟨3239:rvotna⟩2.0.co;2

Marsh, R., Nurser, A. J. G., Megann, A. P., & New, A. L. (2000). Water Mass Transformation in the Southern Ocean of a Global Isopycnal Coordinate GCM. *Journal of Physical Oceanography*, *30*(5), 1013–1045. doi: 10.1175/1520-0485(2000)030⟨1013:wmtits⟩2.0.co;2

Marshall, D. P., & Adcroft, A. J. (2010). Parameterization of ocean eddies: Potential vorticity mixing, energetics and Arnold's first stability theorem. *Ocean Modelling*, *32*, 188-–204. doi: 10.1016/j.ocemod.2010.02.001

Marshall, G. J. (2003). Trends in the Southern Annular Mode from Observations and Reanalyses. *Journal of Climate*, *16*(24), 4134–4143. doi: 10.1175/1520-0442(2003)016⟨4134:titsam⟩2.0.co;2

Marshall, J., & Speer, K. (2012). Closure of the meridional overturning circulation through Southern Ocean upwelling. *Nature Geoscience*, *5*(3), 171–180. doi: 10.1038/ngeo1391

Menviel, L., Timmermann, A., Timm, O. E., & Mouchet, A. (2010). Climate and biogeochemical response to a rapid melting of the West Antarctic Ice Sheet during interglacials and implications for future climate. *Paleoceanography*, *25*(4). doi: 10.1029/2009pa001892

Mohrmann, M., Heuzé, C., & Swart, S. (2021). Southern Ocean polynyas in CMIP6 models. *The Cryosphere*, *15*(9), 4281–4313. doi: 10.5194/tc-15-4281-2021

Moorman, R., Morrison, A. K., & Hogg, A. M. (2020). Thermal Responses to Antarctic Ice Shelf Melt in an Eddy-Rich Global Ocean–Sea Ice Model. *Journal of Climate*, *33*(15), 6599–6620. doi: 10.1175/JCLI-D-19-0846.1

Morrison, A. K., England, M. H., & Hogg, A. M. (2015). Response of Southern Ocean Convection and Abyssal Overturning to Surface Buoyancy Perturbations. *Journal of Climate*, *28*(10), 4263–4278. doi: 10.1175/jcli-d-14-00110.1

Morrison, A. K., Waugh, D. W., Hogg, A. M., Jones, D. C., & Abernathey, R. P. (2022). Ventilation of the Southern Ocean Pycnocline. *Annual Review of Marine Science*, *14*(1), 405–430. doi: 10.1146/annurev-marine-010419-011012

Newsom, E. R., Bitz, C. M., Bryan, F. O., Abernathey, R., & Gent, P. R. (2016). Southern Ocean Deep Circulation and Heat Uptake in a High-Resolution Climate Model. *Journal of Climate*, *29*(7), 2597–2619. doi: 10.1175/JCLI-D-15-0513.1

Nissen, C., Timmermann, R., Hoppema, M., Gürses, O., & Hauck, J. (2022). Abruptly attenuated carbon sequestration with Weddell Sea dense waters by 2100. *Nature Communications*, *13*(1), 3402. doi: 10.1038/s41467-022-30671-3

Nurser, A. J. G., Marsh, R., & Williams, R. G. (1999). Diagnosing Water Mass Formation from Air–Sea Fluxes and Surface Mixing. *Journal of Physical Oceanography*, *29*(7), 1468–1487. doi: 10.1175/1520-0485(1999)029⟨1468:dwmffa⟩2.0.co;2

Nycander, J., Hieronymus, M., & Roquet, F. (2015). The nonlinear equation of state of sea water and the global water mass distribution. *Geophysical Research Letters*, *42*(18), 7714–7721. doi: 10.1002/2015gl065525

Olbers, D., & Visbeck, M. (2005). A Model of the Zonally Averaged Stratification and Overturning in the Southern Ocean. *Journal of Physical Oceanography*, *35*(7), 1190–1205. doi: 10.1175/jpo2750.1

Orsi, A., Johnson, G., & Bullister, J. (1999). Circulation, mixing, and production of Antarctic Bottom Water. *Progress in Oceanography*, *43*(1), 55–109. doi: 10.1016/s0079-6611(99)00004-x

Orsi, A. H., Smethie, W. M., & Bullister, J. L. (2002). On the total input of Antarctic waters to the deep ocean: A preliminary estimate from chlorofluorocarbon measurements. *Journal of Geophysical Research: Oceans*, *107*(C8), 31–1-31-14. doi: 10.1029/2001jc000976

Palter, J. B., Griffies, S. M., Samuels, B. L., Galbraith, E. D., Gnanadesikan, A., & Klocker, A. (2014). The Deep Ocean Buoyancy Budget and Its Temporal Variability. *Journal of Climate*, *27*(2), 551–573. doi: 10.1175/jcli-d-13-00016.1

Paolo, F. S., Fricker, H. A., & Padman, L. (2015). Volume loss from Antarctic ice shelves is accelerating. *Science*, *348*(6232), 327–331. doi: 10.1126/science.aaa0940

Pauling, A. G., Bitz, C. M., Smith, I. J., & Langhorne, P. J. (2016). The Response of the Southern Ocean and Antarctic Sea Ice to Freshwater from Ice Shelves in an Earth System Model. *Journal of Climate*, *29*(5), 1655–1672. doi: 10.1175/jcli-d-15-0501.1

Pellichero, V., Sallée, J.-B., Chapman, C. C., & Downes, S. M. (2018). The southern ocean meridional overturning in the sea-ice sector is driven by freshwater fluxes. *Nature Communications*, *9*(1), 1789. doi: 10.1038/s41467-018-04101-2

Pierce, D. W., Gleckler, P. J., Barnett, T. P., Santer, B. D., & Durack, P. J. (2012). The fingerprint of human-induced changes in the ocean's salinity and temperature fields. *Geophysical Research Letters*, *39*(21). doi: 10.1029/2012GL053389

Purich, A., England, M. H., Cai, W., Sullivan, A., & Durack, P. J. (2018). Impacts of Broad-Scale Surface Freshening of the Southern Ocean in a Coupled Climate Model. *Journal of Climate*, *31*(7), 2613 – 2632. doi: 10.1175/jcli-d-17-0092.1

Purkey, S. G., & Johnson, G. C. (2010). Warming of Global Abyssal and Deep Southern Ocean Waters between the 1990s and 2000s: Contributions to Global Heat and Sea Level Rise Budgets. *Journal of Climate*, *23*(23), 6336–6351. doi: 10.1175/2010jcli3682.1

Purkey, S. G., & Johnson, G. C. (2012). Global Contraction of Antarctic Bottom Water between the 1980s and 2000s. *Journal of Climate*, *25*(17), 5830–5844.

doi: 10.1175/jcli-d-11-00612.1

Purkey, S. G., & Johnson, G. C. (2013). Antarctic Bottom Water Warming and Freshening: Contributions to Sea Level Rise, Ocean Freshwater Budgets, and Global Heat Gain. *Journal of Climate*, *26*(16), 6105–6122. doi: 10.1175/jcli-d-12-00834.1

Redi, M. H. (1982). Oceanic isopycnal mixing by coordinate rotation. *Journal of Physical Oceanography*, *12*, 1154–1158. doi: 10.1175/1520-0485(1982)012⟨1154:OIMBCR⟩2.0.CO;2

Riahi, K., Rao, S., Krey, V., Cho, C., Chirkov, V., Fischer, G., ... Rafaj, P. (2011). RCP 8.5—A scenario of comparatively high greenhouse gas emissions. *Climatic Change*, *109*, 33–57. doi: 10.1007/s10584-011-0149-y

Rignot, E., Jacobs, S., Mouginot, J., & Scheuchl, B. (2013). Ice-Shelf Melting Around Antarctica. *Science*, *341*(6143), 266–270. doi: 10.1126/science.1235798

Rignot, E., Mouginot, J., Scheuchl, B., Broeke, M. v. d., Wessem, M. J. v., & Morlighem, M. (2019). Four decades of Antarctic Ice Sheet mass balance from 1979–2017. *Proceedings of the National Academy of Sciences of the United States of America*, *116*(4), 1095–1103. doi: 10.1073/pnas.1812883116

Rintoul, S. R. (2007). Rapid freshening of Antarctic Bottom Water formed in the Indian and Pacific oceans. *Geophysical Research Letters*, *34*(6). doi: 10.1029/2006gl028550

Rintoul, S. R. (2018). The global influence of localized dynamics in the Southern Ocean. *Nature*, *558*(7709), 209–218. doi: 10.1038/s41586-018-0182-3

Roemmich, D., Church, J., Gilson, J., Monselesan, D., Sutton, P., & Wijffels, S. (2015). Unabated planetary warming and its ocean structure since 2006. *Nature Climate Change*, *5*(3), 240–245. doi: 10.1038/nclimate2513

Russell, J. L., Dixon, K. W., Gnanadesikan, A., Stouffer, R. J., & Toggweiler, J. R. (2006). The Southern Hemisphere Westerlies in a Warming World: Propping Open the Door to the Deep Ocean. *Journal of Climate*, *19*(24), 6382–6390. doi: 10.1175/jcli3984.1

Sallée, J.-B. (2018). Southern Ocean Warming. *Oceanography*, *31*(2). doi: 10.5670/oceanog.2018.215

Sallée, J.-B., Pellichero, V., Akhoudas, C., Pauthenet, E., Vignes, L., Schmidtko, S., ... Kuusela, M. (2021). Summertime increases in upper-ocean stratification and mixed-layer depth. *Nature*, *591*(7851), 592–598. doi: 10.1038/s41586-021-03303-x

Sarmiento, J. L., Gruber, N., Brzezinski, M. A., & Dunne, J. P. (2004). High-latitude controls of thermocline nutrients and low latitude biological productivity. *Nature*, *427*(6969), 56–60. doi: 10.1038/nature02127

Sarmiento, J. L., Hughes, T. M. C., Stouffer, R. J., & Manabe, S. (1998). Simulated response of the ocean carbon cycle to anthropogenic climate warming. *Nature*, *393*(6682), 245–249. doi: 10.1038/30455

Schloesser, F., Friedrich, T., Timmermann, A., DeConto, R. M., & Pollard, D. (2019). Antarctic iceberg impacts on future Southern Hemisphere climate. *Nature Climate Change*, *9*(9), 672–677. doi: 10.1038/s41558-019-0546-1

Schmidtko, S., Heywood, K. J., Thompson, A. F., & Aoki, S. (2014). Multidecadal warming of Antarctic waters. *Science*, *346*(6214), 1227–1231. doi: 10.1126/science.1256117

Sigman, D. M., Hain, M. P., & Haug, G. H. (2010). The polar ocean and glacial cycles in atmospheric CO_2 concentration. *Nature*, *466*(7302), 47–55. doi: 10.1038/nature09149

Silvano, A., Rintoul, S. R., Peña-Molino, B., Hobbs, W. R., Wijk, E. v., Aoki, S., ... Williams, G. D. (2018). Freshening by glacial meltwater enhances melting of ice shelves and reduces formation of Antarctic Bottom Water. *Science Advances*, *4*(4), eaap9467. doi: 10.1126/sciadv.aap9467

Sloyan, B. M., & Rintoul, S. R. (2001). The Southern Ocean Limb of the Global Deep Overturning Circulation. *Journal of Physical Oceanography*, *31*(1), 143–173. doi: 10.1175/1520-0485(2001)031⟨0143:TSOLOT⟩2.0.CO;2

Smith, B., Fricker, H. A., Gardner, A. S., Medley, B., Nilsson, J., Paolo, F. S., ... Zwally, H. J. (2020). Pervasive ice sheet mass loss reflects competing ocean and atmosphere processes. *Science*, *368*(6496), 1239–1242. doi: 10.1126/science.aaz5845

Snow, K., Hogg, A. M., Sloyan, B. M., & Downes, S. M. (2016). Sensitivity of Antarctic Bottom Water to Changes in Surface Buoyancy Fluxes. *Journal of Climate*, *29*(1), 313–330. doi: 10.1175/jcli-d-15-0467.1

Speer, K., Rintoul, S. R., & Sloyan, B. (2000). The Diabatic Deacon Cell. *Journal of Physical Oceanography*, *30*(12), 3212–3222. doi: 10.1175/1520-0485(2000)030⟨3212:tddc⟩2.0.co;2

Speer, K., & Tziperman, E. (1992). Rates of Water Mass Formation in the North Atlantic Ocean. *Journal of Physical Oceanography*, *22*(1), 93–104.

Spence, P., Griffies, S. M., England, M. H., Hogg, A. M., Saenko, O. A., & Jourdain, N. C. (2014). Rapid subsurface warming and circulation changes of Antarctic coastal waters by poleward shifting winds. *Geophysical Research Letters*, *41*(13), 4601–4610. doi: 10.1002/2014gl060613

Spence, P., Sebille, E. v., Saenko, O. A., & England, M. H. (2014). Using Eulerian and Lagrangian Approaches to Investigate Wind-Driven Changes in the Southern Ocean Abyssal Circulation. *Journal of Physical Oceanography*, *44*(2), 662–675. doi: 10.1175/jpo-d-13-0108.1

Stewart, A., & Thompson, A. (2015). The Neutral Density Temporal Residual Mean overturning circulation. *Ocean Modelling*, *90*, 44–56. doi: 10.1016/j.ocemod.2015.03.005

Stouffer, R. J., Seidov, D., & Haupt, B. J. (2007). Climate Response to External Sources of Freshwater: North Atlantic versus the Southern Ocean. *Journal of Climate*, *20*(3), 436–448. doi: 10.1175/jcli4015.1

Swart, N. C., & Fyfe, J. C. (2012). Observed and simulated changes in the Southern Hemisphere surface westerly wind-stress. *Geophysical Research Letters*, *39*(16). doi: 10.1029/2012gl052810

Talley, L. D. (2008). Freshwater transport estimates and the global overturning circulation: Shallow, deep and throughflow components. *Progress in Oceanography*, *78*(4), 257-303. doi: 10.1016/j.pocean.2008.05.001

Talley, L. D. (2013). Closure of the global overturning circulation through the indian, pacific, and southern oceans: Schematics and transports. *Oceanography*, *26*(1). Retrieved from `10.5670/oceanog.2013.07`

Talley, L. D., Reid, J. L., & Robbins, P. E. (2003). Data-Based Meridional Overturning Streamfunctions for the Global Ocean. *Journal of Climate*, *16*(19), 3213–3226. doi: 10.1175/1520-0442(2003)016⟨3213:dmosft⟩2.0.co;2

Tziperman, E. (1986). On the Role of Interior Mixing and Air-Sea Fluxes in Determining the Stratification and Circulation of the Oceans. *Journal of Physical Oceanography*, *16*(4), 680–693. doi: 10.1175/1520-0485(1986)016⟨0680:otroim⟩2.0.co;2

Urakawa, L. S., Tsujino, H., Nakano, H., Sakamoto, K., Yamanaka, G., & Toyoda, T. (2020). The sensitivity of a depth-coordinate model to diapycnal mixing induced by practical implementations of the isopycnal tracer diffusion scheme. *Ocean Modelling*, *154*, 101693. doi: 10.1016/j.ocemod.2020.101693

van Wijk, E. M., & Rintoul, S. R. (2014). Freshening drives contraction of Antarctic Bottom Water in the Australian Antarctic Basin. *Geophysical Research Letters*, *41*(5), 1657–1664. doi: 10.1002/2013gl058921

Walin, G. (1982). On the relation between sea-surface heat flow and thermal circulation in the ocean. *Tellus*, *34*(2), 187–195. doi: 10.1111/j.2153-3490.1982.tb01806.x

Watson, A. J., Schuster, U., Shutler, J. D., Holding, T., Ashton, I. G. C., Landschützer, P., ... Goddijn-Murphy, L. (2020). Revised estimates of ocean-atmosphere CO2 flux are consistent with ocean carbon inventory. *Nature Communications*, *11*(1), 4422. doi: 10.1038/s41467-020-18203-3

Waugh, D. W., Hogg, A. M., Spence, P., England, M. H., & Haine, T. W. (2019). Response of Southern Ocean ventilation to changes in mid-latitude westerly winds Response of Southern Ocean ventilation to changes in mid-latitude westerly winds. *Journal of Climate*, *32*(17), 5345–5361. doi: 10.1175/jcli-d-19-0039.1

Waugh, D. W., Primeau, F., DeVries, T., & Holzer, M. (2013). Recent Changes in the Ventilation of the Southern Oceans. *Science*, *339*(6119), 568–570. doi: 10.1126/science.1225411

Zhang, L., Delworth, T. L., Cooke, W., Goosse, H., Bushuk, M., Morioka, Y., & Yang, X. (2021). The Dependence of Internal Multidecadal Variability in the Southern Ocean on the Ocean Background Mean State. *Journal of Climate*, *34*(3), 1061–1080. doi: 10.1175/jcli-d-20-0049.1

Zhang, L., Delworth, T. L., Cooke, W., & Yang, X. (2019). Natural variability of Southern Ocean convection as a driver of observed climate trends. *Nature Climate Change*, *9*(1), 59–65. doi: 10.1038/s41558-018-0350-3

Zhang, L., Delworth, T. L., & Jia, L. (2017). Diagnosis of Decadal Predictability of Southern Ocean Sea Surface Temperature in the GFDL CM2.1 Model. *Journal of Climate*, *30*(16), 6309–6328. doi: 10.1175/jcli-d-16-0537.1

Zhang, L., Delworth, T. L., Kapnick, S., He, J., Cooke, W., Wittenberg, A. T., ... Morioka, Y. (2022). Roles of Meridional Overturning in Subpolar Southern Ocean SST Trends: Insights from Ensemble Simulations. *Journal of Climate*, *35*(5), 1577–1596. doi: 10.1175/jcli-d-21-0466.1